On the combined flow and structural measurements via robotic volumetric PTV

M A Mitrotta, Francesco; Sodja, Jurij; Sciacchitano, Andrea

DOI
10.1088/1361-6501/ac41dd

Publication date
2022

Document Version
Final published version

Published in
Measurement Science and Technology

Citation (APA)
M A Mitrotta, F., Sodja, J., & Sciacchitano, A. (2022). On the combined flow and structural measurements via robotic volumetric PTV. *Measurement Science and Technology*, *33*(4), Article 045201. https://doi.org/10.1088/1361-6501/ac41dd

Important note
To cite this publication, please use the final published version (if applicable).
Please check the document version above.

On the combined flow and structural measurements via robotic volumetric PTV

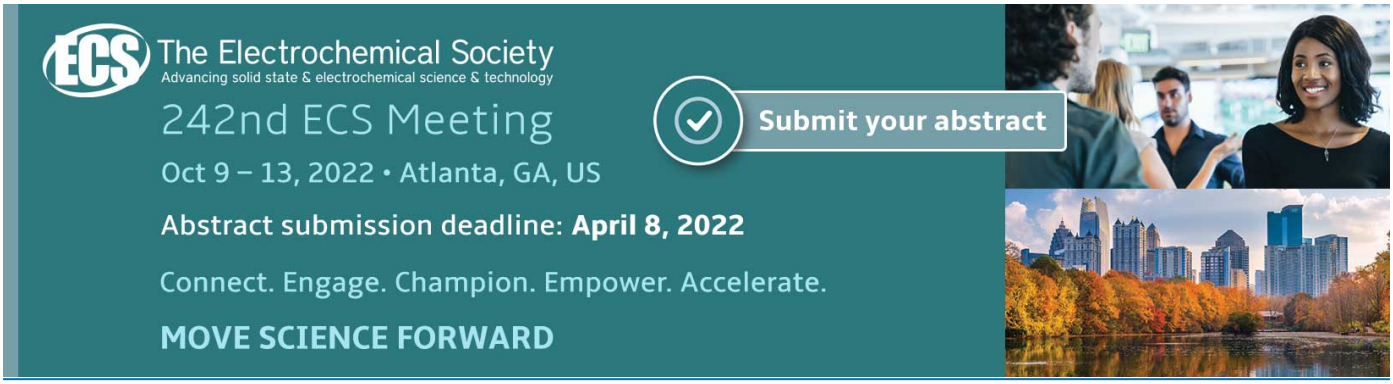

OPEN ACCESS
IOP Publishing
Measurement Science and Technology
Meas. Sci. Technol. **33** (2022) 045201 (22pp)
https://doi.org/10.1088/1361-6501/ac41dd

On the combined flow and structural measurements via robotic volumetric PTV

Francesco M A Mitrotta, Jurij Sodja and Andrea Sciacchitano*

Faculty of Aerospace Engineering, TU Delft, Delft, Netherlands

E-mail: a.sciacchitano@tudelft.nl

Received 25 October 2021, revised 7 December 2021
Accepted for publication 10 December 2021
Published 10 January 2022

Abstract

This study describes a novel measurement approach for combined flow and structural measurements in wind tunnels using robotic volumetric particle tracking velocimetry (PTV). The measurement approach is based on the application of a particle tracking algorithm on images including flow or structure tracers, where the latter are implemented by means of fiducial markers. The main steps of the measurement procedure comprise the simultaneous acquisition of flow and structure tracers in the same images, the distinction of the tracers leading to separate flow and structure image sets, the application of Lagrangian particle tracking and the further post-processing, and recombination of the obtained data. The approach is applied to the fluid-structure interaction between a flexible plate with a span of 1.2 m and a periodic gust. The total measurement volume amounts approximately to 150 liters. A phase-averaged description of the FSI problem is presented, with the focus on the effects of the spatio-temporal averaging of the flow information. The structural displacements obtained from the PTV system are validated against a scanning vibrometer. The phase-averaged displacement of the markers is also analyzed, assessing both the validity of the phase-averaged approach and the physical coherence of their motion with respect to a structural model of the plate. It is found that robotic volumetric PTV is suitable for the measurement of large-scale structural displacements, while it should not be used to measure small-scale vibrations. Finally, a visualization of the combined measurement is presented, together with an analysis of the consistency between the measured structure and flow field.

Keywords: robotic volumetric PTV, HFSB, shake-the-box, aeroelasticity, fluid-structure interaction, wind tunnel

(Some figures may appear in colour only in the online journal)

* Author to whom any correspondence should be addressed.

1. Introduction

In aeroelastic experiments, the interaction between flow and structure governs the studied phenomena. For this reason, static and dynamic measurements of the flow field around the experimental model and of its structural response are needed. A relevant requirement for experiments involving fluid-structure interaction (FSI) is the non-intrusiveness of the measurement system, so as to ensure that the structural properties of the model, the mass distribution of the latter as well as the flow field are not altered by the measurement apparatus (Ricketts 1990).

A variety of measurement devices has been used over the years in aeroelastic experiments. In 1990, strain gauges, potentiometers, accelerometers, and gyros were reported to be used for structural assessments. The awareness of the need for a proper flow characterization for the understanding of aeroelastic phenomena was already present at that time. However, pressure transducers were the main tool for unsteady aerodynamic measurements, as quantitative flow visualization techniques were not yet mature enough (Ricketts 1990).

Although in the last decades particle image velocimetry (PIV) has emerged as the main technique for quantitative flow visualization in wind tunnels (Adrian and Westerweel 2011, Raffel *et al* 2018), its use in modern aeroelastic experiments involving large-scale test models is still very limited. Pressure transducers are still employed as the main tool for unsteady aerodynamic measurements and structural characterization is still performed by means of strain gauges and accelerometers, leading to complex instrumentation of wind tunnel models (see e.g. the work of Ballmann *et al* 2008, Mai *et al* 2011, Silva *et al* 2012). However, optical marker tracking has been introduced for the measurement of structural displacements, enabling a non-intrusive characterization of the test model's static and dynamic structural response (see e.g. the PicColor system used by Ballmann *et al* 2008, Mai *et al* 2011).

Only a few studies can be found in the literature reporting the combination of quantitative flow visualization by means of PIV and optical structural measurements in wind or water tunnels. Among those, the technique most frequently coupled to PIV is digital image correlation (DIC) (Timpe *et al* 2013, Bleischwitz *et al* 2017, Marimon Giovannetti *et al* 2017, Zhang *et al* 2019). In these studies, DIC was used to measure the two- or three-dimensional displacement field of the investigated test model. Regarding the flow measurements, they were always limited to a plane and frequently to two components of the velocity field, except for the work of Marimon Giovannetti *et al* (2017), who measured three velocity components in one plane via the use of a stereoscopic PIV setup.

Volumetric flow measurement was only achieved in the work of Kalmbach and Breuer (2013) by means of the V3V system. However, the structural characterization was performed with a multiple-point triangulation sensor rather than with a DIC system, leading to the measurement of displacements only along a two-dimensional profile.

Besides the rare availability of volumetric flow measurements, the mentioned works present flow and structural measurements over domains of the order of 0.1×0.1 m^2, thus covering only a small fraction of the size of the models typically used in wind tunnels for aerospace research and development. Conversely, a large variety of aeroelastic phenomena, such as flutter and dynamic response to gusts, involves the presence of 3D unsteady flows and large-scale structures, making volumetric flow and structural measurements over large domains crucial for a holistic investigation of such FSI problems.

Furthermore, the combined flow and structural characterization was always achieved with two separate measurement systems. This led to complex setups such as the ones of Bleischwitz *et al* (2017) and Marimon Giovannetti *et al* (2017), with challenges related to the synchronization of the two systems and their optical separation. Hence, a combined approach that allows to simultaneously measure the flow field and structural deformation in aeroelastic problems using a single system is currently missing.

In the last years, volumetric PIV experiments have seen a significant increase in the size of the measurement volume. The reason is twofold. First, the introduction of helium-filled soap bubbles (HFSB) for PIV experiments in wind tunnels demonstrated the availability of flow tracers with a larger scattering area in comparison to the traditional micron size particles (Scarano *et al* 2015). Second, the development of advanced Lagrangian particle tracking (LPT) algorithms such as shake-the-box (STB) has made the processing of the PIV images for volumetric measurements more computationally affordable compared to traditional tomographic reconstruction techniques (Schanz *et al* 2016).

The recent introduction of robotic volumetric particle tracking velocimetry (PTV) by Jux *et al* (2018) has permitted to exploit the potential of HFSB and STB even further, thereby revealing the capability of time-averaged three-dimensional wind tunnel measurements in volumes of several cubic meters. Robotic volumetric PTV is based on the robotic control of a coaxial volumetric velocimetry (CVV) probe (Schneiders *et al* 2018) together with the use of HFSB as flow tracers and STB as the processing algorithm. The robotic control of the probe is used to partition a large measurement volume into a number of smaller volumes. Independent acquisitions are performed for each volume. The data is then processed by STB and recombined on a global reference frame thanks to the positional information provided by the robotic system. Finally, an ensemble average is performed over the entire measurement volume, yielding the time-averaged flow field. For periodic phenomena, the technique can be extended to obtain phase-averaged flow fields, as demonstrated by Martínez Gallar *et al* (2019).

This work introduces a novel measurement approach to obtain combined flow and structural measurements in a wind tunnel using robotic volumetric PTV, performing for the first time a thorough analysis of the spatial and temporal resolutions achievable for periodic problems, whereby a phase-averaged analysis becomes feasible. The fundamental idea of this approach is to use the same particle tracking algorithm employed to track flow tracers also for the tracking of structural markers. The principles of the measurement process are

first explained in detail, while a wind tunnel experiment is used for demonstration and validation.

2. Measurement procedure

The proposed measurement procedure relies on the application of fiducial markers onto the structure's surface. These are used as tracers of the structural motion in an analogous way to the particles employed as tracers of the flow. The steps of the measurement process are summarized in figure 1 and explained in more detail below.

Step 1—Image acquisition. Images including both flow and structure tracers are sequentially acquired with the CVV probe for each volume comprising the measurement domain. Acquisitions are carried out in a time-resolved fashion for the subsequent application of an LPT algorithm.

Step 2—Tracers separation. The hypothesis for the separation of flow and structure tracers is analogous to the one made by Sciacchitano and Scarano (2014) and relies on the fact that the velocity of a structural element is typically much lower than the flow velocity. As a result, when conducting a time-resolved measurement with sufficiently high resolution to sample the motion of both flow and structure, a structural marker resides at the same pixel location for several time instants, contrary to flow tracers that occupy a pixel only in one time instant and not in the preceding or successive ones. When this hypothesis holds, the application of a high pass filter allows to obtain an image set including only flow tracers, while the application of a low pass filter results in an image set including only structure tracers. The Nyquist frequency sampling criterion can be used to determine the minimum acquisition frequency needed to resolve the desired flow and structural time scales.

Step 3—Lagrangian tracking. The images acquired with the CVV probe are processed to determine, in the Lagrangian sense, the position and velocity of each particle in time. Both flow tracers and surface markers are tracked independently using the LPT algorithm STB, developed by Schanz *et al* (2016). It should be noticed that, due to the different nature of the tracers, the flow and the structure data sets require distinct optical transfer functions (OTF, Schanz *et al* 2012). The same volume self-calibration (Wieneke 2008) can be used for both image sets. Besides, with the aim of using the same calculation chain to extract both the flow and the structural motion (volume self-calibration, OTF, and STB), the shape and size of the structural markers are chosen such that their images resemble the ones of the HFSB. Using structural markers of different shapes and/or sizes with respect to the flow tracers would also be possible; however, this possibility is left to future investigations.

Step 4—Tracks data reduction. In principle, the tracks obtained from the Lagrangian tracking can be combined to visualize the instantaneous flow field and structural motion. For periodic problems, the phase-average approach is often beneficial to suppress the measurement noise and enhance the spatial resolution. In this regard, common preliminary steps comprise the mapping of the tracks' positional data from the local reference frames of the acquisition volumes to a global reference frame and the identification of the phases corresponding to the time instants of the tracked particles. As far as the flow tracks are concerned, basic (Jux *et al* 2018) or advanced (Agüera *et al* 2016) ensemble averaging methods can be employed to obtain an Eulerian description of the flow. An extension to phase average applications of the approach presented by Agüera *et al* (2016) is discussed in section 3.2. On the structure side, the processing of the Lagrangian tracks results in the phase-averaged description of the markers' displacement, thus allowing the characterization of the dynamic structural response.

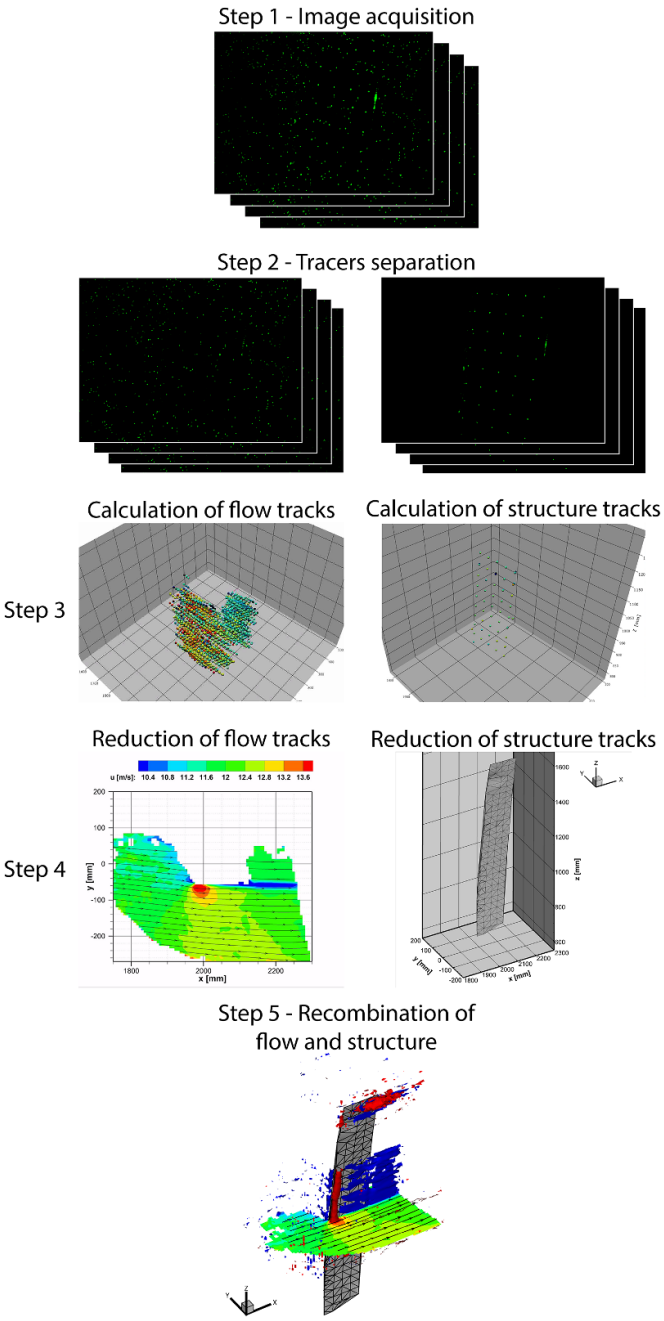

Figure 1. Schematic workflow of the measurement process.

Step 5—Recombination of flow and structure. The phase-averaged descriptions of flow and structure are combined together, both for visualization and further analysis purposes. This recombination step is straightforward as the two descriptions use the same global reference frame.

3. Lagrangian tracks analysis

This section discusses the analysis of Lagrangian tracks for the case of a periodic FSI problem, considering both the flow tracer particles and structural fiducial markers.

3.1. Mapping of measurement time to phases

The application of LPT to both sets of flow and structure images results in a Lagrangian description of positions and velocities of flow particles and markers. When a periodic FSI phenomenon is considered, a triple decomposition can be applied to each data point representing a certain flow or structural characteristic u:

$$u = \overline{u} + \tilde{u} + u', \tag{1}$$

where $\overline{u}$ represents the time-averaged value, $\tilde{u}$ the quasi-periodic component and u' the random fluctuations caused by turbulence for example (Kalmbach and Breuer 2013). When dealing with measurement data, u' contains also the contribution of random measurement errors.

The summation of the global mean component $\overline{u}$ with the quasi-periodic part $\tilde{u}$ represents the phase-averaged term $\langle u \rangle$, so that (1) reads:

$$u = \langle u \rangle + u'. \tag{2}$$

As a consequence, it is necessary to define a processing strategy for the Lagrangian tracks to calculate the term $\langle u \rangle$ and to obtain a phase-averaged description of the studied phenomenon. The first step consists in mapping the absolute time of the tracks onto a non-dimensional time corresponding to the phase of the average cycle, which requires the knowledge of the period or the frequency of the periodic phenomenon. In fact, for periodic FSI problems it is possible to identify a characteristic frequency, which is the inverse of the period. The large scales in the flow and the structure follow this characteristic frequency. The knowledge of this frequency or of the associated period allows to resolve the phase-averaged large scales of the flow and the structural motions. The frequency can be either known *a priori*, as in the case of a forced harmonic excitation, or it can be determined *a posteriori* analyzing the measured deflection or deformation of the structure (Kalmbach and Breuer 2013).

The mentioned mapping can be summarized by the following expression:

$$u(x,y,z,t) \rightarrow u(x,y,z,\phi = t/T - N_c(t)), \tag{3}$$

where ϕ is the non-dimensional time of the average cycle, bounded between 0 and 1, T is the reference period of the periodic phenomenon and N_c is the number of complete cycles occurred at time t.

3.2. Flow tracks

The Lagrangian description of the flow can be transformed into an Eulerian description employing the ensemble averaging technique. This involves the discretization of the measurement volume into small cubic cells, also called interrogation bins, followed by the averaging of the instantaneous velocity of the particles falling inside each cell. In this way a time-averaged velocity field is obtained and different approaches are available for this purpose. For example, Jux *et al* (2018) applied a simple averaging in space, which can also be referred to as a top-hat filter. Agüera *et al* (2016) proposed two more advanced methods to reduce the modulation effects caused by spatial averaging: the Gaussian filter and the polynomial fit.

For phase-averaged flow fields, these methods can be extended to the temporal dimension, becoming in this way spatio-temporal ensemble averaging methods. Analogously to the spatial bin with a linear size l_B, a temporal bin with size ϕ_B has to be defined. This temporal bin consists of a non-dimensional time window centered around a selected phase value so that only the particles falling inside the spatial bin and the prescribed temporal window are considered for the ensemble average.

The temporal information of the particles, which is mapped to the phases of the cycle, is used to add a time-dependent component to the weights of the Gaussian filter and the terms of the polynomial functions. The idea behind this is to benefit from the temporal dimension to increase the achievable spatial resolution. In fact, by increasing the temporal bin size it is possible to reduce the size of the spatial bin, thereby increasing the spatial resolution of the measurement.

The extension of the polynomial fit method is considered here, being the method used for the experiment presented in section 4. For a second-order polynomial, the velocity distribution inside the interrogation bin can be expressed as:

$$\begin{aligned}\langle u \rangle = {} & a_0 + a_1\Delta x + a_2\Delta y + a_3\Delta z + a_4\Delta x^2 \\ & + a_5\Delta x\Delta y + a_6\Delta y^2 + a_7\Delta x\Delta z + a_8\Delta y\Delta z \\ & + a_9\Delta z^2 + a_{10}\Delta\phi + a_{11}\Delta x\Delta\phi + a_{12}\Delta y\Delta\phi \\ & + a_{13}\Delta z\Delta\phi + a_{14}\Delta\phi^2,\end{aligned} \tag{4}$$

where $(\Delta x, \Delta y, \Delta z)$ indicate the spatial distance from the bin centroid and $\Delta\phi$ the temporal separation from the considered phase of the cycle. Similarly to Agüera *et al* (2016), the unknown coefficients can be calculated by finding the least-square solution of the system of equations formulated using the positional, temporal, and velocity information of the particles falling inside the spatio-temporal bin. The mean velocity is taken from the value at the centroid of the spatio-temporal bin, and the standard deviation $\sigma_{\langle u \rangle}$ is calculated by taking into account the polynomial weighting of the velocity distribution.

The uncertainty of the phase-averaged velocity $\epsilon_{\langle u \rangle}$ depends on the velocity fluctuations due to turbulence and random measurement errors, both included in the standard deviation, and on the number of uncorrelated samples N_{unc} used for the calculation of the mean (Sciacchitano and Wieneke 2016):

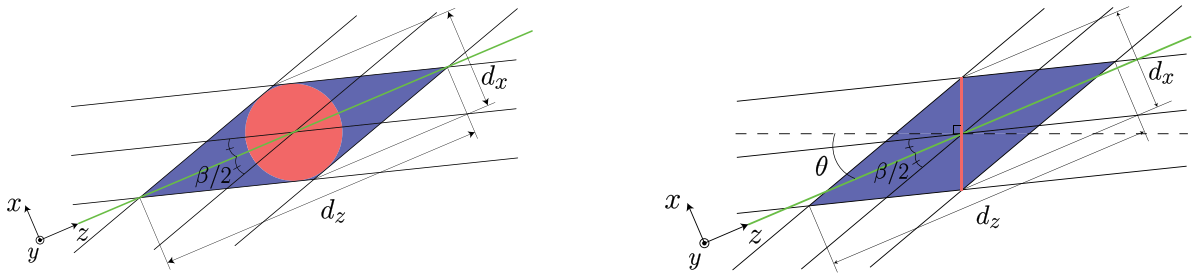

(a) Flow particle. (b) Marker.

Figure 2. Schematic illustration of the top view of the reconstructed particle for flow and structure tracers. Actual tracers in red, reconstructed particle in blue, z-axis of CVV system in green.

$$\epsilon_{\langle u \rangle} = \frac{k\sigma_{\langle u \rangle}}{\sqrt{N_{unc}}}, \tag{5}$$

where k is the coverage factor. The random measurement errors include also the errors related to the phase detection process. A conservative estimate of N_{unc} is obtained by dividing the observation time with the integral time-scale of the flow, which may be taken as the average period of the studied phenomenon.

3.3. Structure tracks

The application of Lagrangian tracking on the structure images results in the instantaneous description of the markers' position. The related uncertainty can be analyzed following the model discussed by Schneiders *et al* (2018). For a CVV system, the instantaneous positional uncertainty of a particle along the coaxial (z) direction is $2/\beta$ times larger than the one along the in-plane directions x and y, β being the tomographic aperture:

$$\epsilon_z = \frac{2}{\beta}\epsilon_x. \tag{6}$$

Considering that in the imaging regime of CVV the magnification factor varies significantly within the measurement volume, both the uncertainties ϵ_x and ϵ_z depend on the distance z, with ϵ_z presenting a much larger variation due to the tomographic angle β, which is also dependent on z.

The proportional uncertainty model (Adrian 1991) used by Schneiders *et al* (2018) for 3D particles can be applied to two-dimensional surface markers as well, with the difference that the aspect ratio of the imaged surface marker varies with the viewing direction. In fact, while the ideal spherical shape of a flow tracer allows to reconstruct the same elongated particle regardless of where it is imaged from, this does not apply for a surface marker, as long as its size is not diffraction-limited. As a consequence, in addition to the distance z from the probe, the positional uncertainty is also affected by the orientation of the probe, since it influences the size of the reconstructed particle along both the in-plane and the coaxial directions.

This can be observed in figure 2, where the three-dimensional reconstructions of a flow and a structure tracer are compared, assuming the use of circular surface markers. It is evident that for the latter the shape and size of the reconstructed surface marker change with the angle θ, which defines the orientation of the CVV system with respect to the marker's normal direction. It should be noticed that the robotic control of the CVV probe allows to determine a full three-dimensional orientation of the probe relative to the marker, implying a more complex set of misalignment angles describing the shape and size of the reconstructed particle. For the sake of simplicity and intending to provide just an approximate estimate of the positional uncertainty of the markers, only the misalignment identified by the angle θ is considered here to derive an expression relating the uncertainty of the surface markers to the viewing direction.

Using the proportional uncertainty model proposed by Adrian (1991), the relation between the positional uncertainties along the x- and the z-direction can be expressed in general as:

$$\epsilon_z = \epsilon_x \frac{d_z}{d_x}, \tag{7}$$

where d_x and d_z are the reconstructed particle sizes along the x- and the z-axis, respectively. These sizes can be found for the reconstructed structure tracer analyzing the geometry of the triangle constituting the first half of the parallelogram shown in figure 2(b). According to the derived geometrical relations, the ratio d_z/d_x reads:

$$\frac{d_z}{d_x} = \frac{\cos\delta}{\cos\theta}\left(\frac{2}{\sin^2\beta}\left(\cos^2(\beta/2-\theta) + \cos^2(\beta/2+\theta)\right) - 1\right)^{1/2}, \tag{8}$$

where the angle δ is obtained as:

$$\delta = \tan^{-1}\left(\tan^2\frac{\beta}{2}\tan\theta\right). \tag{9}$$

The reader is referred to appendix A for the derivation of these relations.

Figure 3 shows the variation of the uncertainties ϵ_x and ϵ_z along the z-axis for different values of θ. A marker with a diameter of 1.5 mm is considered, together with the properties of the CVV system used by Schneiders *et al* (2018). The marker size is based on the size of the markers used in the

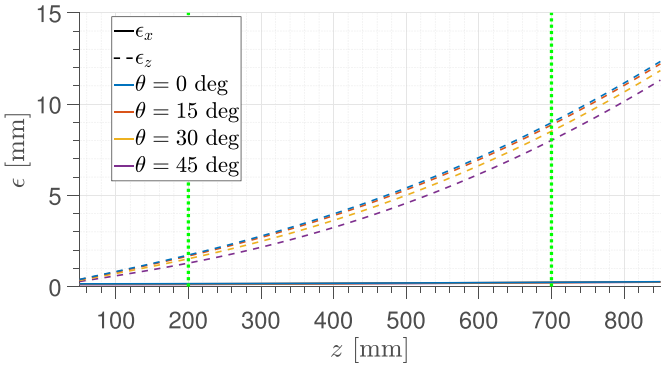

Figure 3. Positional uncertainty of a marker with $d_p = 1.5$ mm for the CVV system used by Schneiders *et al* (2018). Bounds of the typical range of operation of the CVV system in green.

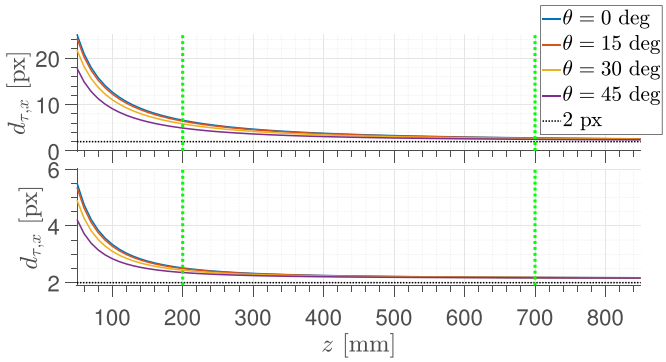

Figure 4. Variation of the particle image diameter along the z-axis of the probe for markers with a physical diameter of 1.5 mm (top) and 0.3 mm (bottom). CVV system used by Schneiders *et al* (2018) is considered. Bounds of the typical range of operation of the CVV system in green.

experiment presented in section 4. It can be observed that by increasing the angle θ, the size of the reconstructed particle along the z-axis decreases and consequently also the associated positional uncertainty. The same effect occurs along the x-axis, although it remains bounded within 0.5 mm. Considering that the CVV probe operates at distances between 200 and 700 mm and angles up to 45 degrees (Jux *et al* 2018), ϵ_z can be expected to vary between 1 and 9 mm, while ϵ_x will be in the order of 0.1–0.2 mm.

It should be noticed that according to the characteristics of the employed CVV system, there may be some limitations related to the physical size of the marker. The proportional uncertainty model becomes unreliable when the particle image size falls below 2 pixels and other sources of uncertainties, such as peak locking, become more important. As a consequence, it may be useful to assess the range of acceptable distance z and angle θ which ensures that a marker of a given physical diameter covers the minimum required amount of pixels in the images.

Figure 4 shows the variation of the particle image size $d_{\tau,x}$ in pixels along the coaxial direction for markers with a physical diameter of 1.5 and 0.3 mm, the latter corresponding to the nominal size of an HFSB. As expected, the particle image size decreases asymptotically to the diffraction-limited diameter. Close to the probe, a large difference between the two markers can be observed, caused by the dominant geometrical component of the particle image diameter. As the diffraction-limited diameter becomes more important, the difference in the number of pixels reduces. Besides, also the difference between different viewing angles for the same marker size appears to decrease with the distance from the probe.

In the presented case, both physical sizes ensure an image size above the threshold of 2 pixels. However, if the requirement for the minimum number of pixels is increased, e.g. to 3 pixels, then using a marker size equal to the size of the flow particles would not satisfy such a requirement over the entire operating range of the probe, while this would be possible over most of the range with a bigger marker. As far as the viewing angle is concerned, no particular restriction appears to be needed in the operating range from 0 to 45 degrees.

An undesired but typical feature of the marker tracking process consists in the interruption of the reconstructed marker track at one or several time instants, thus resulting in multiple tracks for the same marker. The main cause of this can be found in the positional uncertainty of the tracked marker, which results in a measurement noise that can disrupt the particle tracking algorithm, leading to the interruption of the track. This occurrence hinders a straightforward analysis of the instantaneous characteristics of the markers during an acquisition period since it is first necessary to identify the tracks associated with the same marker and then join them in a unique track. The operation of tracks connection has to be carried out before the phase identification step described in section 3.1. Different approaches are possible; the one used for the experiment presented in section 4 is discussed in appendix B.

Furthermore, when assessing the instantaneous displacement of a marker, it is possible to reduce the measurement error employing the technique of track regularization. This consists in the application of a sliding regression of a second or higher-order polynomial (i.e. a Savitzky-Golay filter, Savitzky and Golay 1964) through the measured particle positions. The measurement error is expected to reduce proportionally to $\sqrt{N_p/P}$ with respect to the displacement at largest time separation $(N_p - 1)\Delta t$, where N_p is the number of particles taking part in the regression, P is the order of the polynomial and Δt is the pulse separation time (Lynch and Scarano 2013). The use of track regularization for the reduction of the markers' measurement error is demonstrated on the experimental data in section 5.2.

Once a unique track has been assembled for each marker and the temporal information has been mapped to the phases of the cycle, the phase-averaging of the displacements can take place. When different acquisitions are considered, it is also necessary to merge the information of corresponding markers. In order to reduce the measurement error, the mentioned technique of track regularization can be embedded in the averaging process. Analogously to the flow velocity, the standard deviation of the markers' displacement is calculated by taking into account the polynomial weighting introduced by the

sliding regression. The reader is referred to appendix B for further details about the embedding of track regularization in the phase-averaging process.

4. Setup of the wind tunnel experiments

A wind tunnel investigation is carried out in order to demonstrate the proposed measurement approach and assess the related accuracy. A flexible plate excited by a continuous harmonic gust is selected as a test case. In this way, the periodic flow field and structural displacements can be measured in a phase-averaged fashion.

4.1. Experimental setup

The experimental investigation is carried out in the Open Jet Facility of TU Delft. This is a closed-loop, open test section wind tunnel with an octagonal outlet section of $2.85 \times 2.85\ \mathrm{m}^2$. A gust generator is used to attain a periodic flow field in the wind tunnel. The design and characterization of the gust generator are reported in detail by Lancelot *et al* (2017a, 2017b).

The chosen test object is a rectangular plate with a 1217.5 mm span, a 170 mm chord, and a 2.5 mm thickness. It is made of aluminum alloy 7075, with a density of $2810\ \mathrm{kg\ m^{-3}}$ and a Young modulus of 71.7 GPa. The plate is painted black with grey circular markers of 1.5 mm in diameter. The tests are performed at wind tunnel speeds of 11 and 12 m s^{-1}, corresponding to a chord-based Reynolds number between 1.3×10^5 and 1.4×10^5.

The robotic volumetric PTV system used in the present experimental investigation employs a *LaVision MiniShaker Aero* CVV probe mounted on a *universal Robots—UR5* robotic arm. The light source is provided by a *Quantronix Darwin-Duo* Nd-YLF laser, having a light wavelength $\lambda = 527$ nm and pulse energy of 2×25 mJ at a pulsation frequency of 1 kHz. The seeding of HFSB in the flow is provided by a seeding rake developed by the Aerodynamic section of TU Delft's Aerospace Faculty. This rake is composed of ten wings with 20 bubble generators each, and it is placed in the settling chamber of the wind tunnel to increase the particle concentration in the test section and to minimize the turbulence intensity generated by the rake itself. With the described configuration, the average value of particle per pixel for the images obtained in the experimental tests amounts to 0.0018. A summary of the technical specification of the overall system is given in table 1.

The structural measurements obtained from the robotic volumetric PTV system are validated using a laser Doppler vibrometer, the *Polytec PSV-500 Scanning Vibrometer*[1], which can determine the vibration velocity at a selected point, as well as displacement and acceleration through temporal integration and differentiation, respectively. According to technical specifications reported by the manufacturer, the resolution of the measured velocity is 14 μm s^{-1}.

Table 1. Technical specifications of the robotic volumetric PTV system used in the experiment.

Optics	
Focal length	4 mm
Numerical aperture	11
Imaging	
Horizontal β ($z_0 = 400$ mm)	8 deg
Vertical β ($z_0 = 400$ mm)	4 deg
Active sensor size	640 px × 475 px
Pixel pitch	4.8 μm
Magnification ($z_0 = 400$ mm)	0.01
Bit depth	10
Seeding	
Seeded cross-section	$0.5 \times 0.95\ \mathrm{m}^2$
Control device	*LaVision* fluid supply unit
Software	
Acquisition & processing	*LaVision* DaVis 10.0.5

A complete overview of the experimental setup in the wind tunnel is given in figure 5, together with the reference frame used for the PTV acquisitions and the marker arrangement. It can be noticed how the scanning vibrometer (SV) is placed on the opposite side of the test object with respect to the robotic volumetric PTV system in order to avoid light source contamination.

4.2. Data acquisition procedures

In order to study the response of the aluminum plate to a continuous gust excitation, a continuous harmonic gust is generated in the flow by the gust generator. The robotic volumetric PTV system and the SV are synchronized with the gust generator using a common trigger signal. Additionally, electric signals representing the angle of the gust vanes and the measurement instants of the two systems are recorded by means of a *National Instrument* acquisition station controlled by a purpose-developed interface in the LabVIEW environment. These signals are used later for the phase identification step.

Three different measurement sets are acquired during the experiment. The related physical and acquisition parameters are summarized in table 2. The first set consists of simultaneous robotic volumetric PTV and SV acquisition, without HFSB seeding. This offers a clean validation case for the structural measurements. For the second measurement set, the HFSB generator is switched on. This is done to assess the capability of the robotic volumetric PTV system to deliver valid structural measurement in the presence of flow tracers. Finally, for the third measurement set, the SV is switched off and the robotic volumetric PTV system is used to investigate the dynamic structural response to the gust over the entire span of the plate.

The PTV volumes acquired for the different measurement sets are shown in figure 6. It can be observed that only three selected volumes along the span are measured for the first two

[1] The system used is a *PSV-500-B* with a *PSV-I-550 Scanning Head Xtra*. Technical specifications are available at https://www.polytec.com/eu/vibrometry/products/full-field-vibrometers/psv-500-scanning-vibrometer (accessed: 16 September 2021).

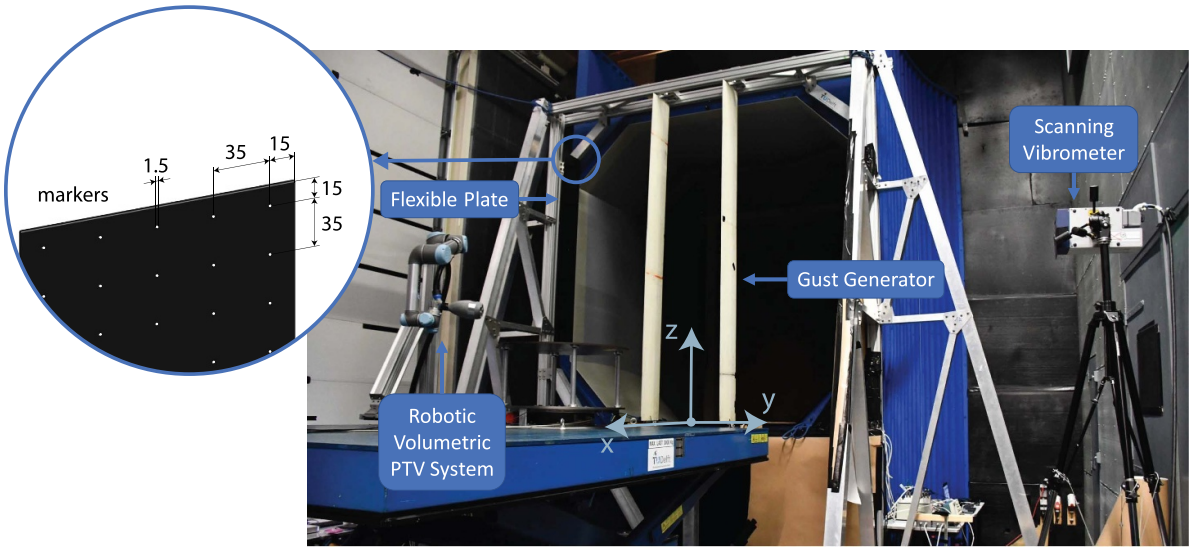

Figure 5. Illustration of the experimental setup. Dimensions of markers arrangement in millimeters.

Table 2. Physical and acquisition parameters of the studied measurement cases.

	PTV-SV	PTV-SV-HFSB	PTV-HFSB
Physical parameters			
Wind tunnel speed (m s^{-1})	11	11	12
Gust frequency (Hz)	0.9	0.9	1.0
Gust vanes deflection (deg)	5	5	10
Acquisition parameters			
PTV acquisition frequency (Hz)	200	821.7	821.7
SV acquisition frequency (Hz)	1000	1000	
# gust cycles per acquisition	20	20	20
# PTV images per acquisition	4400	18 076	16 433
# PTV volumes	3	3	14
# acquisitions per PTV volume	1	1	8
# SV samples per acquisition	2200	2200	
# SV points	9	6	

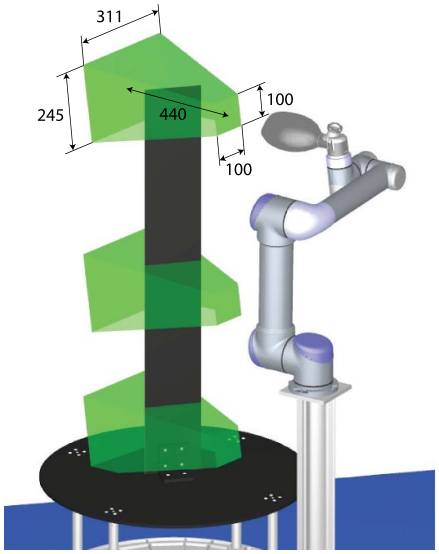

(a) Volumes for the PTV-SV and PTV-SV-HFSB sets. The indicated dimensions of the CVV volume are only approximate.

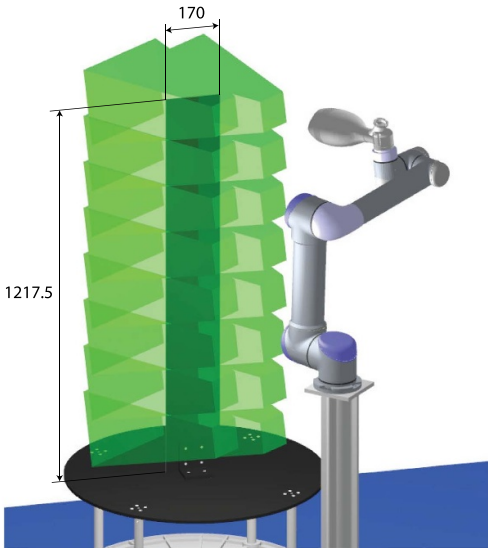

(b) Volumes for the PTV-HFSB set.

Figure 6. Illustration of the PTV volumes acquired during the experiment and of the size of the flexible plate. All dimensions in millimeters.

data sets. The total measurement volume for the third data set amounts to approximately 150 liters. Finally, additional acquisitions are performed with the PTV system to measure the static position of the markers in wind-tunnel-off conditions and for the two wind tunnel speeds tested.

5. Results

5.1. Flow field

The technique for the reduction of flow tracks discussed in section 3.2 is demonstrated here, using a second-order polynomial. At first, the effect of the spatial bin variation is assessed without the use of any temporal information. Afterward, the use of different temporal bin sizes is discussed. All comparisons are performed using the PTV-HFSB data set, considering a horizontal plane cutting the plate at half of its span at phase $\phi = 0$ and employing a bin overlap factor of 75%.

5.1.1. Effect of spatial bin size. Four spatial bin sizes are investigated: 85.0, 42.5, 28.3, and 17.0 mm, respectively corresponding to 1/2, 1/4, 1/6, and 1/10 of the plate's chord c. Since no temporal information is considered, only the spatial terms of equation (4) are used for the regression inside the interrogation bins. For each phase, only the particles falling within a non-dimensional time window corresponding to the interval between two consecutive image recordings are considered. Each bin of the Cartesian grid is populated only when at least 20 particles are found, otherwise the bin is considered invalid.

The resulting contour of the streamwise velocity is shown in figure 7 together with the surface of the plate, which is obtained from the triangulation of the measured markers. The investigated flow field shows two interesting features: a region of accelerated flow close to the plate's leading edge and a region of decelerated flow in the wake of the plate.

As expected, it is possible to notice how a larger bin size allows to obtain valid results in a bigger portion of the measured volume, given the higher probability of filling the interrogation bins with the required minimum number of particles. However, this happens at the cost of spatial modulation of the velocity. In particular, the wake behind the trailing edge of the plate is not captured. At the same time, the velocity fields obtained with smaller bins are noisier, as small nonphysical accelerations and decelerations can be detected along the streamlines. However, higher spatial resolution is achieved, resulting in higher streamwise velocity at the suction peak, and a better definition of the wake. For $l_B = c/10$, most bins include less than 20 particles, and therefore are considered invalid and blanked out.

The effect of bin size on the spatial resolution of velocity can be further assessed by looking at the velocity profiles along the y-axis. Two locations are chosen, $x/c = 11.65$ and $x/c = 12.82$ (see figure 7(a)), in order to encompass the accelerated flow region and the wake, respectively. The resulting profiles are shown in figure 8, where it can be observed how a smaller spatial bin size allows to achieve a higher spatial resolution at the cost of an increased noise level of the mean field. This is especially evident for the velocity profiles cutting through the wake, showing a larger velocity deficit as the bin size is reduced.

5.1.2. Effect of temporal bin size. The benefit of using temporal information is demonstrated on a spatial bin size of $l_B = c/10$, which was found to be too small to obtain valid results in a meaningful portion of the measurement volume using only spatial information. Four different temporal bin sizes are investigated: 1/32, 1/16, 1/4, and 1/2 of the cycle period. All terms of equation (4) are used for the regression. To consider a bin valid, the minimum number of particles inside each spatio-temporal bin is increased to 30, in order to keep it double the number of coefficients of the regression. Furthermore, for each phase the interrogation bins are considered invalid if no particle is found within a non-dimensional time window corresponding approximately to the interval between two consecutive image recordings. This is done to calculate only the portion of the flow field that is truly measurable by the CVV probe at the considered phase. In fact, the results would include a portion of the flow field beyond the plate for large time kernels if the mentioned bin detection feature was not employed. Such an effect would be caused by the fact that the motion of the plate becomes significant for relatively large time intervals and it modifies the boundary of the flow particles' shadow region.

Figure 9 shows the streamwise velocity contours resulting from the different temporal bin sizes. It is possible to observe that in comparison to figure 7(d), the use of $l_B = c/10$ combined with temporal information returns a rather full velocity field. This means that the use of temporal information successfully allows to increase the spatial resolution when binning Lagrangian tracks in a phase average fashion. Some regions with discontinuities are visible, especially in the upper left corner of the plots. These are caused by the fact that in some bins the number of particles of the ensemble is below the threshold value. Those bins are blanked, thus causing the observed discontinuities. Furthermore, it can be observed that smaller temporal bin sizes produce noisier mean velocity fields, similarly to what was noticed for the variation of the spatial bin size.

The same velocity profiles previously investigated are studied again to assess the effect of temporal bin size on the spatial distribution of velocity. The plots of the velocity profiles are shown in figure 10, where an increase of the velocity peak in the accelerated flow region and of the velocity deficit in the wake can be noticed as the time kernel is reduced. These results also show a higher spatial resolution compared to the results of figure 8 for $\phi_B = 1/16$ and $1/32$ of the period. At the same time, the velocity profile obtained for $\phi_B = 1/2$ of the period suggests that an excessive extension of the time kernel leads to temporal modulation, which affects the spatial distribution of the velocity field.

Temporal modulation can also be assessed by looking at the change of streamwise velocity over the cycle. Similarly to the analysis of the velocity profiles, two points on the considered

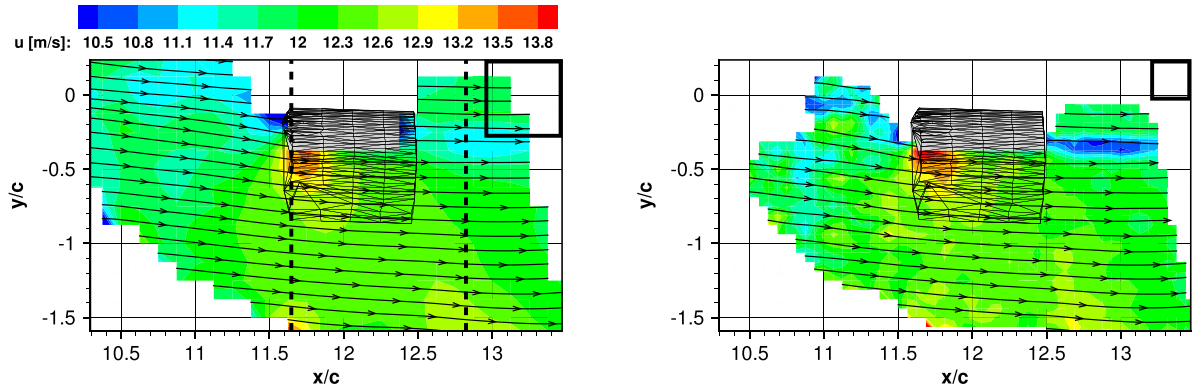

(a) $l_B = c/2$. The vertical lines show the location of the velocity profiles analyzed in Figures 8 and 10.

(b) $l_B = c/4$.

(c) $l_B = c/6$.

(d) $l_B = c/10$.

Figure 7. Comparison of the streamwise velocity contour for different spatial bin sizes. The size of the averaging bins is shown as a square in the top right corner of each plot.

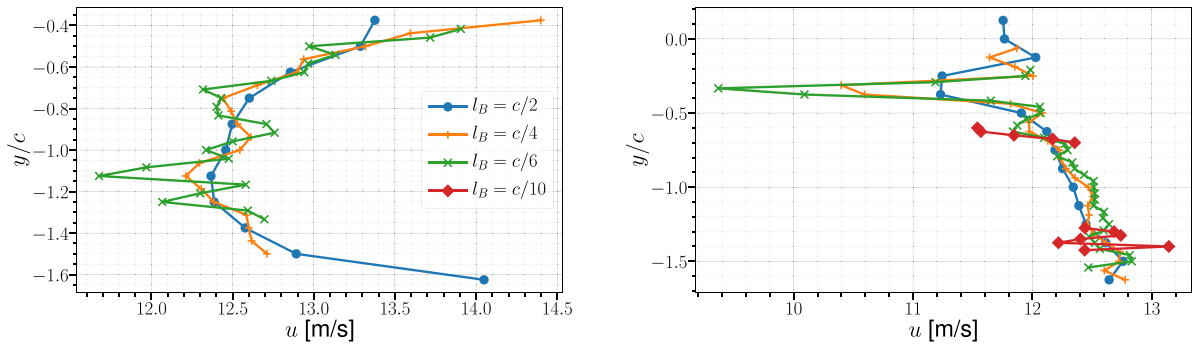

(a) Accelerated flow region.

(b) Wake.

Figure 8. Comparison of the streamwise velocity profile along the y-axis for different spatial bin sizes.

plane are chosen, $[x/c, y/c] = [11.65, -0.41]$ and $[x/c, y/c] = [12.82, -0.35]$ (see figure 9(a)), in the accelerated flow region and in the wake, respectively.

The resulting temporal velocity profiles are shown in figure 11. The temporal modulation is evident for $\phi_B = 1/2$ since a smaller maximum velocity in the accelerated flow region and a larger minimum velocity in the wake are observed with respect to the other temporal bin sizes. Furthermore, similarly to what was noticed for the spatial velocity distribution, the temporal profiles show a smoother evolution over the cycle for larger temporal bin sizes.

In conclusion, it is evident that it is possible to benefit from the temporal dimension to increase the achievable spatial resolution. In fact, enlarging the temporal bin size it is possible to reduce the size of the spatial bin so that a similar number of particles is caught inside the spatio-temporal bin for the calculation of the phase-averaged velocity. However, the choice of the temporal bin size has to result from a trade-off among desired spatial resolution, smoothness of mean flow field, and temporal modulation of the velocity. From the presented results, it can be inferred that temporal bins larger than 1/4 of the cycle period should be avoided in order

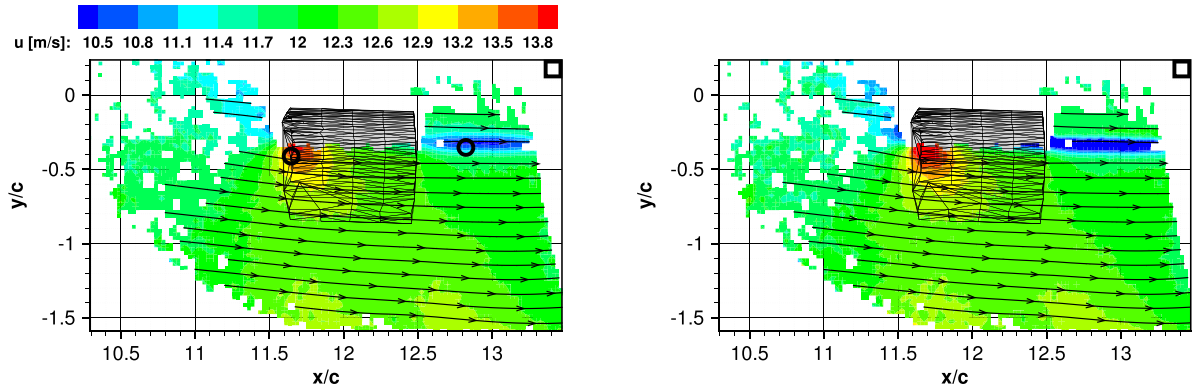

(a) $\phi_B = 1/2$. The circles show the locations the change of velocity over the cycle is analyzed (see Figure 11).

(b) $\phi_B = 1/4$.

(c) $\phi_B = 1/16$.

(d) $\phi_B = 1/32$.

Figure 9. Comparison of the streamwise velocity contour for different temporal bin sizes. The size of the averaging bins is shown as a square in the top right corner of each plot.

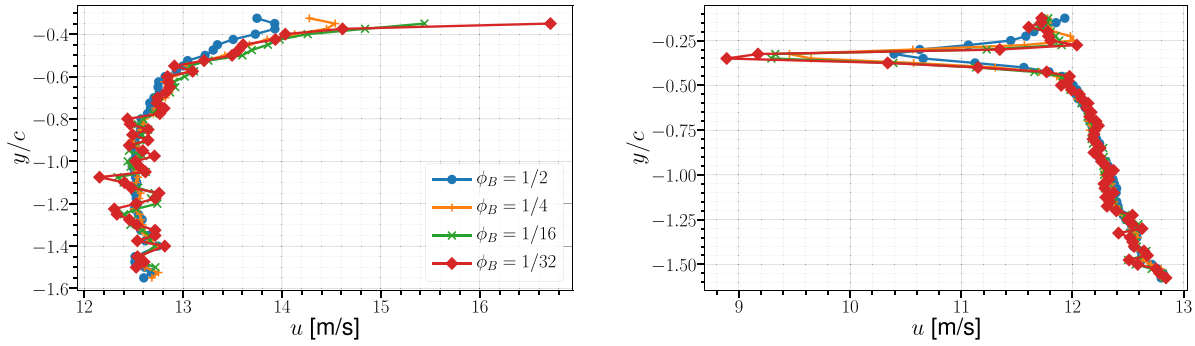

(a) Accelerated flow region.

(b) Wake.

Figure 10. Comparison of the streamwise velocity profile along the y-axis for different temporal bin sizes.

not to incur modulation effects such as the observed reduction of the velocity deficit in the wake.

5.2. Structural measurement validation

In this section, the structural measurements of the robotic volumetric PTV system are validated against the measurements of the SV. First, a validation of the instantaneous structural displacements is performed. Afterward, the quality of the phase-averaged approach is discussed. In this regard, two aspects are considered: the measurement of a single marker and the consistency of multiple markers for the representation of the entire structure.

5.2.1. Instantaneous results. The validation of the instantaneous structural measurements is performed using the data obtained from the PTV-SV measurement set. Three markers along the span of the plate are selected: one at the tip (96% of the span), one at the center (49%), and one at the root (9%) of the plate. All markers are located at the center of the chord

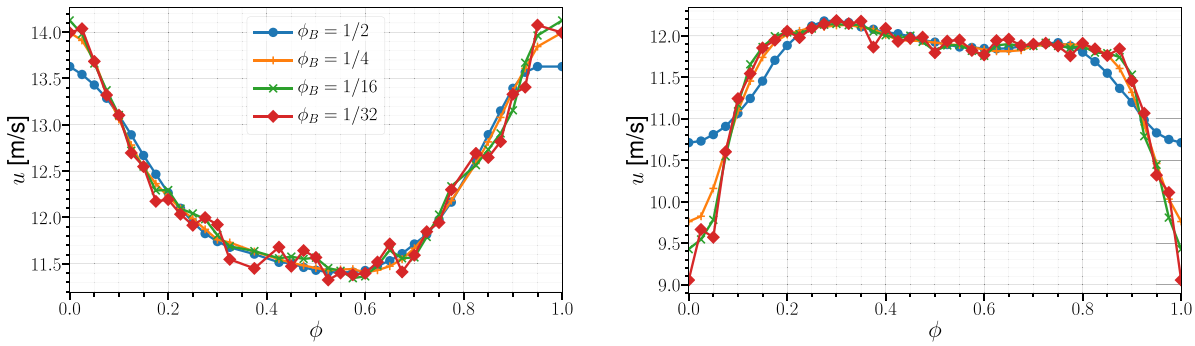

(a) Accelerated flow region. (b) Wake.

Figure 11. Comparison of the streamwise velocity during the average cycle at selected points for different temporal bin sizes.

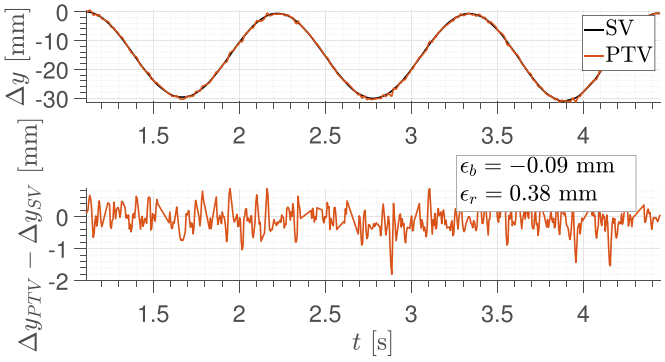

Figure 12. Time history of the instantaneous displacement measured by robotic volumetric PTV and SV for the midspan marker (top) and of the related error (bottom). Only results from 3 gust cycles are shown.

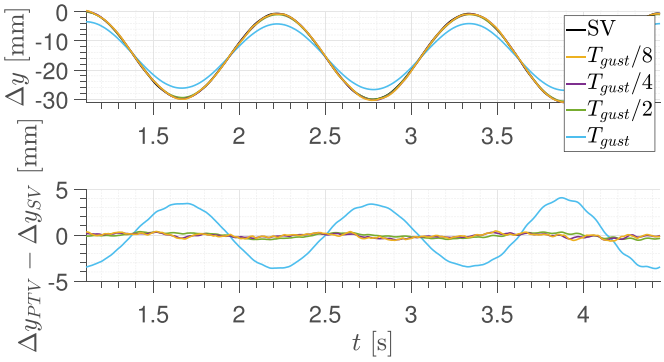

Figure 13. Time history of the instantaneous displacement obtained with different time kernel settings for the Savitzky-Golay filter on robotic volumetric PTV data for the midspan marker. Comparison with SV measurement (top) and related error (bottom). Only results from 3 gust cycles are shown.

and are measured one at a time by the synchronized robotic volumetric PTV and SV systems.

Figure 12 shows the comparison of the instantaneous displacements of the midspan marker measured by the two systems. The displacement shown in the plot is the one along the y-axis of the PTV measurement reference frame (see figure 5), corresponding to the surface-normal displacement measured by the SV. The analyzed displacement is relative to the first detected position of the marker. The reference measurement (SV) exhibits a harmonic response with an amplitude of 30 mm and a frequency of 0.9 Hz, which corresponds to the gust frequency. The PTV measurement is found to be in good agreement with the reference.

The bias error $\epsilon_{b,\Delta y}$ and the random error $\epsilon_{r,\Delta y}$ of the PTV measurement relative to the SV measurement are respectively calculated as the mean and the standard deviation of the difference between the PTV and the SV measurements. For the calculation of this difference, the displacements of the SV are linearly interpolated to the time instants of the PTV measurement. The values resulting from 20 gust cycles are $\epsilon_{b,\Delta y} \approx -0.09$ mm and $\epsilon_{r,\Delta y} \approx 0.38$ mm, respectively corresponding to 0.3% and 1.3% of the average displacement amplitude.

Considering an approximate distance of 400 mm between the probe and the plate and an orientation angle of 30 degrees, the experimental random error appears to be in between the values predicted for ϵ_x and ϵ_z according to the analysis of section 3.3, so between 0.17 mm and 3.63 mm, even if closer to the former value. This can be ascribed to the fact that the analyzed motion of the marker has a component both along the coaxial direction and along the in-plane directions of the CVV system, meaning that the observed measurement error is a combination of the measurement errors along each direction.

The PTV results shown in figure 12 are the raw results obtained from the application of the STB algorithm and joining together the tracks belonging to the same marker, which do not include the effect of track regularization. As mentioned in section 3.3, the latter concept can be employed to reduce the measurement error. For this purpose, a sliding least square regression of a second-order polynomial is applied to the raw PTV displacements of the midspan marker, investigating different time kernels.

Figure 13 shows a comparison among the results for the selected time kernels. Not much difference can be observed among the curves obtained with kernels ranging from 1/8 to 1/2 of the nominal gust period T_{gust}. Modulation of the measured displacements becomes evident only when a kernel of one gust period is used.

The results in terms of bias and random errors are summarized in table 3. Bias and random errors of regularised

Table 3. Bias and random errors for the tracking of the midspan marker for different sizes of the temporal kernel. Δ_ϵ represents the percentage difference between the errors of the raw and the regularized displacements.

Temporal kernel	ϵ_b (mm)	Δ_{ϵ_b} (%)	ϵ_r (mm)	Δ_{ϵ_r} (%)
Raw measurement	−0.09	—	0.38	—
$T_{gust}/8$	−0.10	+5.0	0.25	−35.2
$T_{gust}/4$	−0.10	+4.4	0.20	−47.4
$T_{gust}/2$	−0.09	−0.9	0.21	−44.0
T_{gust}	−0.12	+34.1	2.52	+558.8

displacements are calculated excluding the initial and final part of the signal so that calculations are not affected by side effects of the regression. The exclusion intervals are equal to half the regression kernel. The percentage difference of the errors is calculated as $\Delta_\epsilon = (\epsilon_{regularized} - \epsilon_{raw})/\epsilon_{raw} \times 100$. Up to a kernel of 1/2 of the gust period, the random error sees a substantial decrease compared to the one of the raw measurement, while the bias error stays almost unchanged. For a kernel of one gust period, both bias error and random error experience a strong increase. The best performance in terms of random error is obtained with a kernel of 1/4 of the gust period, resulting in $\epsilon_{b,\Delta y} \approx -0.10$ mm and $\epsilon_{r,\Delta y} \approx 0.20$ mm, respectively 0.3% and 0.7% of the average displacement amplitude.

Besides aerodynamic and elastic loads, another important aspect in aeroelastic experiments is given by inertial loads, which are proportional to the structural acceleration. Therefore, it is important to evaluate the acceleration measurements performed with the robotic volumetric PTV system. The instantaneous acceleration of the markers is calculated from the displacement data of both systems employing a sliding least square regression of a second-order polynomial and deriving the polynomial twice in time. Based on the previous results, a kernel of 1/4 of the gust period is used.

The comparison between the results of robotic volumetric PTV and SV for the midspan marker is shown in figure 14. The two curves are in good agreement, even if the PTV curve appears noisier compared to the SV curve. The bias error amounts to be 0.17 mm s^{-2}, corresponding to 0.02% of the acceleration amplitude (approximately 1100 mm s^{-2}), and the random error amounts to 28.81 mm s^{-2}, which is equal to 2.6% of the acceleration amplitude.

The results of the regularized displacements and accelerations of the remaining markers are summarised in table 4 in terms of bias and random errors. The errors of the tip marker are larger than those of the midspan marker. This can be ascribed to the larger positional uncertainty caused in turn by the larger displacement of the tip marker and thus by a smaller tomographic angle far from the CVV probe. However, when the relative errors are considered, these are of the same order as the ones found for the midspan marker. Conversely, the relative random errors of the root marker are significantly larger. The reason can be found in the displacement amplitude of the marker, which is approximately 0.85 mm. Both from the theoretical predictions of section 3.3 and the experimental evidence, it can be observed that the PTV measurement cannot reliably resolve such a small motion, as the displacement

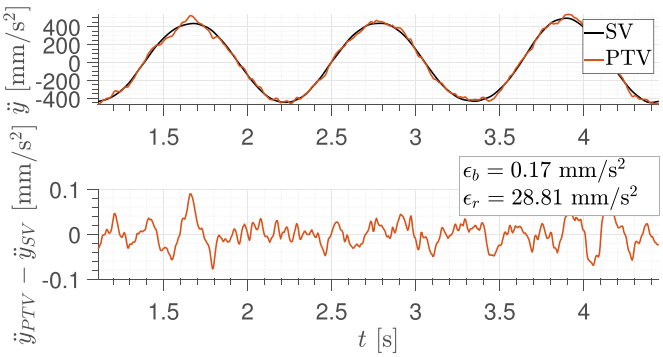

Figure 14. Time history of the instantaneous acceleration obtained from robotic volumetric PTV and SV measurements for the midspan marker (top) and of the related error (bottom). Only results from 3 gust cycles are shown.

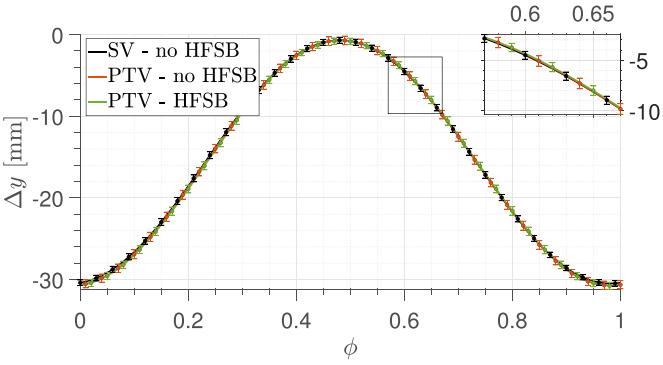

Figure 15. Phase-averaged structural displacements of the midspan marker. The error bars represent one standard deviation.

uncertainty results in the order of 0.5 mm. The reader is referred to appendix C for the displacement and acceleration plots of the tip and root markers.

Overall, looking at the random errors of displacements in table 4, it can be inferred that thanks to the combination of a certain orientation of the probe relative to the markers' motion and the use of track regularization, it is possible to obtain measurement errors closer to the values predicted for the in-plane components of the CVV system (order of 0.1–0.2 mm) rather than the ones predicted for the coaxial component (between 1 and 9 mm).

5.2.2. Phase-averaged results. The scatter from one cycle to the other is considered to evaluate the quality of the phase-averaged approach on an individual marker. Three measurements are compared: SV without HFSB, PTV without HFSB, and PTV with HFSB. The previously considered midspan marker is used here to obtain the phase-averaged displacements over 20 cycles. The results are shown in figure 15, where the scatter among the different cycles is indicated by means of error bars representing one standard deviation around the mean values.

The mean and maximum standard deviation over the average cycle is summarized in table 5. For each phase, the standard deviation stems from the contribution of two

Table 4. Summary of bias and random errors for the three markers. Relative errors are given as a percentage of the amplitude. Track regularization is applied to raw measurements using a time kernel of $T_{gust}/4$.

	Displacements					Accelerations				
	Amplitude	ϵ_b		ϵ_r		Amplitude	ϵ_b		ϵ_r	
Marker	(mm)	(mm)	(%)	(mm)	(%)	(mm s^{-2})	(mm s^{-2})	(%)	(mm s^{-2})	(%)
Root	0.85	0.03	3.5	0.38	44.7	26	−0.24	0.9	47.71	183.5
Midspan	30	−0.10	0.3	0.20	0.7	900	0.17	0.02	28.81	3.2
Tip	90	0.14	0.2	0.72	0.8	2600	0.47	0.02	70.60	2.7

Table 5. Mean and maximum standard deviation of the phase-averaged displacements of the midspan marker over the cycle.

Measurement	$\overline{\sigma_{\Delta y}}$ (mm)	$\sigma_{\Delta y,max}$ (mm)
SV-no HFSB	0.38	0.43
PTV-no HFSB	0.52	0.58
PTV-HFSB	0.45	0.52

components: the scatter from one gust to the other and the random error of the measurement system. It can be noticed that the smallest value for both mean and maximum standard deviation is obtained from the SV measurement, amounting respectively to 1.3% and 1.4% of the displacement amplitude. This can be explained by assuming that the random error of the SV is negligible because of the low measurement uncertainty. As a consequence, the resulting standard deviation can be mainly attributed to the scatter among the gusts generated over the different cycles. The larger standard deviation obtained for the PTV-no HFSB and the PTV-HFSB curves includes a non-negligible contribution given by the random error of the robotic volumetric PTV system. Furthermore, considering the comparable values of the mean and maximum standard deviation of the measurements with and without HFSB, it can be inferred that the introduction of flow particles does not compromise the accuracy of the structural measurement performed with the robotic volumetric PTV system.

5.2.3. Consistency of markers' motion. Complete structural measurements by means of robotic volumetric PTV rely on tracking multiple markers at the same time within a single acquisition and on joining together the results of different acquisitions. For this reason, it is important to evaluate the consistency of the physical motion of markers belonging to the same and different PTV volumes. The assessment is performed here by comparing the position of the phase-averaged markers with a structural model of the plate fitted to the markers themselves. Two PTV volumes belonging to the PTV-SV measurement set and including a group of midspan and tip markers are used for the assessment.

The plate structural model has a time-dependent component describing the temporal evolution during the cycle and a spatial component describing the deformed shape of the flexible plate in the three-dimensional space. Given the harmonic excitation, the temporal component is described by a sine wave, while the spatial part comprises a weighted sum of the first three natural vibration modes, corresponding to the first and second bending mode and the first torsional mode of the plate. The complete deformed shape of the plate in time is then described as follows:

$$\begin{cases} x_i = \sin(2\pi\phi + \xi)\left(\sum_{j=1}^{3} A_j \Delta x_{e_j,i}\right) + x_{s,i} \\ y_i = \sin(2\pi\phi + \xi)\left(\sum_{j=1}^{3} A_j \Delta y_{e_j,i}\right) + y_{s,i} \\ z_i = \sin(2\pi\phi + \xi)\left(\sum_{j=1}^{3} A_j \Delta z_{e_j,i}\right) + z_{s,i}, \end{cases} \tag{10}$$

where $[x_i, y_i, z_i]$ are the coordinates of the ith point of the model at phase ϕ of the cycle, $[\Delta x_{e_j,i}, \Delta y_{e_j,i}, \Delta z_{e_j,i}]$ is the displacement vector corresponding to the jth vibration mode of the plate at the ith point and $[x_{s,i}, y_{s,i}, z_{s,i}]$ are the coordinates of the ith point in the static condition. A_1, A_2, and A_3 are the weights of the different vibration modes and ξ is the phase of the sine wave.

The vibration modes used in equation (10) are obtained from a FE model of the plate using the SOL 103 routine of the commercial software MSC Nastran. The parameters A_1, A_2, A_3, and φ are found minimizing the summation of the squared distance between the markers measured within the two selected PTV volumes and the surface obtained from the triangulation of the points resulting from equation (10). An illustration of the markers and the surface resulting from the regression of the physical model is given in figure 16.

Once the parameters A_1, A_2, A_3, and φ are found, it is possible to evaluate the mean absolute distance of the markers from the surface of the structural model during the cycle. The results are shown in figure 17, where the standard deviation of the distances is also displayed. In the plot, the upper x-axis shows the tip displacement of the plate during the cycle, where the largest positive value indicates the plate's position furthest from the CVV probe and the largest negative value indicates the plate's position closest to the probe.

It can be observed that tip and midspan markers have similar mean distance and standard deviation. In fact, considering the average over the cycle, the distance of both tip and midspan markers from the surface of the structural model is equal to 2.1 ± 1.2 mm. Furthermore, the evolution of the two mean distance curves does not show any evident correlation with the tip displacement. Thus, it can be inferred that the larger positional uncertainty at a larger distance from the probe does not compromise the structural consistency of the tracked markers.

In conclusion, it can be stated that the measured motion of the markers appears to be consistent with a structural model of

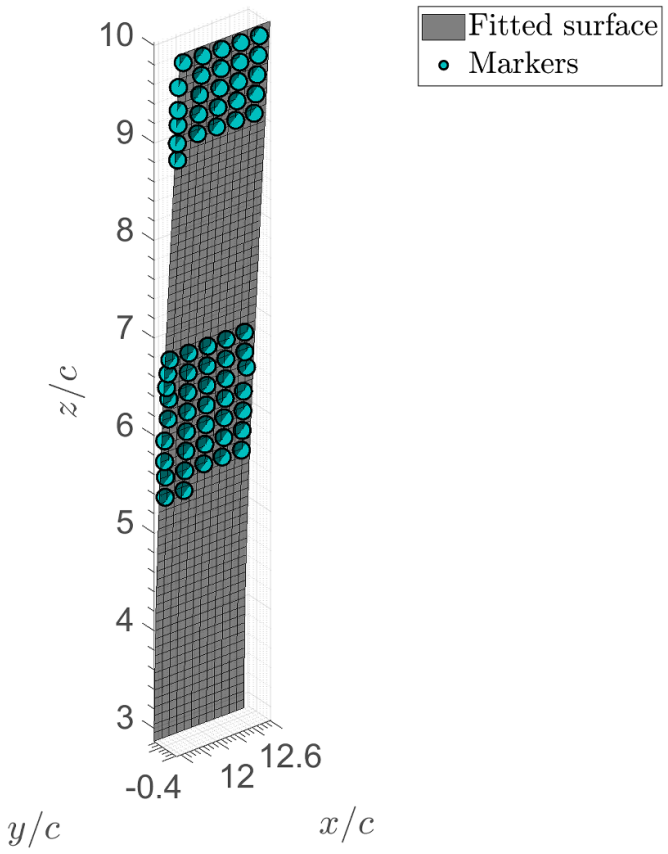

Figure 16. Phase-averaged markers (light blue circles) and fitted surface for phase $\phi = 0$.

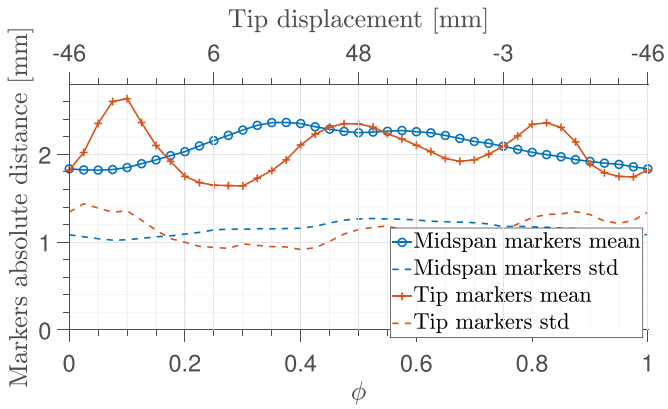

Figure 17. Mean absolute distance and standard deviation between the measured markers and the fitted surface during the average cycle.

the plate based on its first three vibration modes. The position of the majority of the markers deviates at most by 3.3 mm from the surface of the structural model, corresponding to 3.5% of the tip displacement amplitude.

5.3. Fluid-structure visualization

The combination of the phase-averaged description of flow and structure permits to visualize the investigated aeroelastic phenomenon, as shown in figure 18. The results are obtained from the PTV-HFSB measurement set. The phase-averaged markers are found by processing one acquisition for each PTV volume shown in figure 6(b). Regarding the flow, four independent views in the midspan region of the plate and one in the tip region are considered, thus representing only a part of the total measurement volume. At least six acquisitions are used for each view to obtain the results shown in the figure. A spatio-temporal ensemble average is carried out, using a quadratic polynomial fit. The spatial bin size is taken as $l_B = 28.3$ mm, corresponding to 1/6 of the plate chord, while the temporal bin size is taken as $\phi_B = 1/16$ of the cycle. These values are chosen to reduce the mean flow field noise following the guidelines established in section 5.1.

Four different phases of the gust cycle are presented, namely $\phi = 0$, $\phi = 0.25$, $\phi = 0.5$ and $\phi = 0.75$. The 3D view shown in figure 18 contains the plate surface obtained from the measured markers, a slice cut at $z = 1096$ mm (approximately 50% of the plate span) colored with the streamwise component of the velocity u and illustrating the 3D streamlines, and two iso-surfaces of the same velocity component, one for $u = 10.4$ m s^{-1} (corresponding to $u/u_\infty = 0.87$) and the other for $u = 13.8$ m s^{-1} (corresponding to $u/u_\infty = 1.15$). Similarly to figure 9, some discontinuities can be observed in the contour plots, which are caused by bins being blanked due to a smaller number of particles than the threshold value.

It is possible to notice that for phase $\phi = 0$ a coherent region of accelerated flow can be observed over the midspan zone in the proximity of the leading edge of the plate. For the same zone, a coherent region of decelerated flow is formed for phase $\phi = 0.5$. The observed measurements are in line with the expectations: depending on the phase of the cycle, the iso-surface of the accelerated and decelerated flow can be associated with a suction and a pressure side of the plate, respectively. This corresponds to the generation of a lift force that is either opposite or concordant with the y-axis.

The iso-surface of decelerated flow can also be observed for $\phi = 0$ and $\phi = 0.5$ in the wake of the plate, while for the other two phases the velocity contour on the slice reveals a smaller velocity deficit. For the phase $\phi = 0$, the iso-surface of decelerated flow is also visible close to the plate surface, suggesting the presence of a region of separated flow.

As far as the combined measurement is concerned, the results of the different phases suggest that the measured flow field follows coherently the movement of the plate, thus providing a qualitative confirmation of the consistency between the flow and structure measurements.

5.4. Consistency of the fluid-structure measurement

An important aspect of the proposed measurement approach lies in the consistency between the flow and structural results. In order to provide a quantitative assessment of this consistency, the position of the plate's surface, measured through the markers, is compared with the position of the flow particles. Given the orientation of the CVV probe with respect to the plate during the experiment (see figure 6), an ideal measurement producing perfectly consistent results should find flow particles only 'before' the plate, while no particle should be

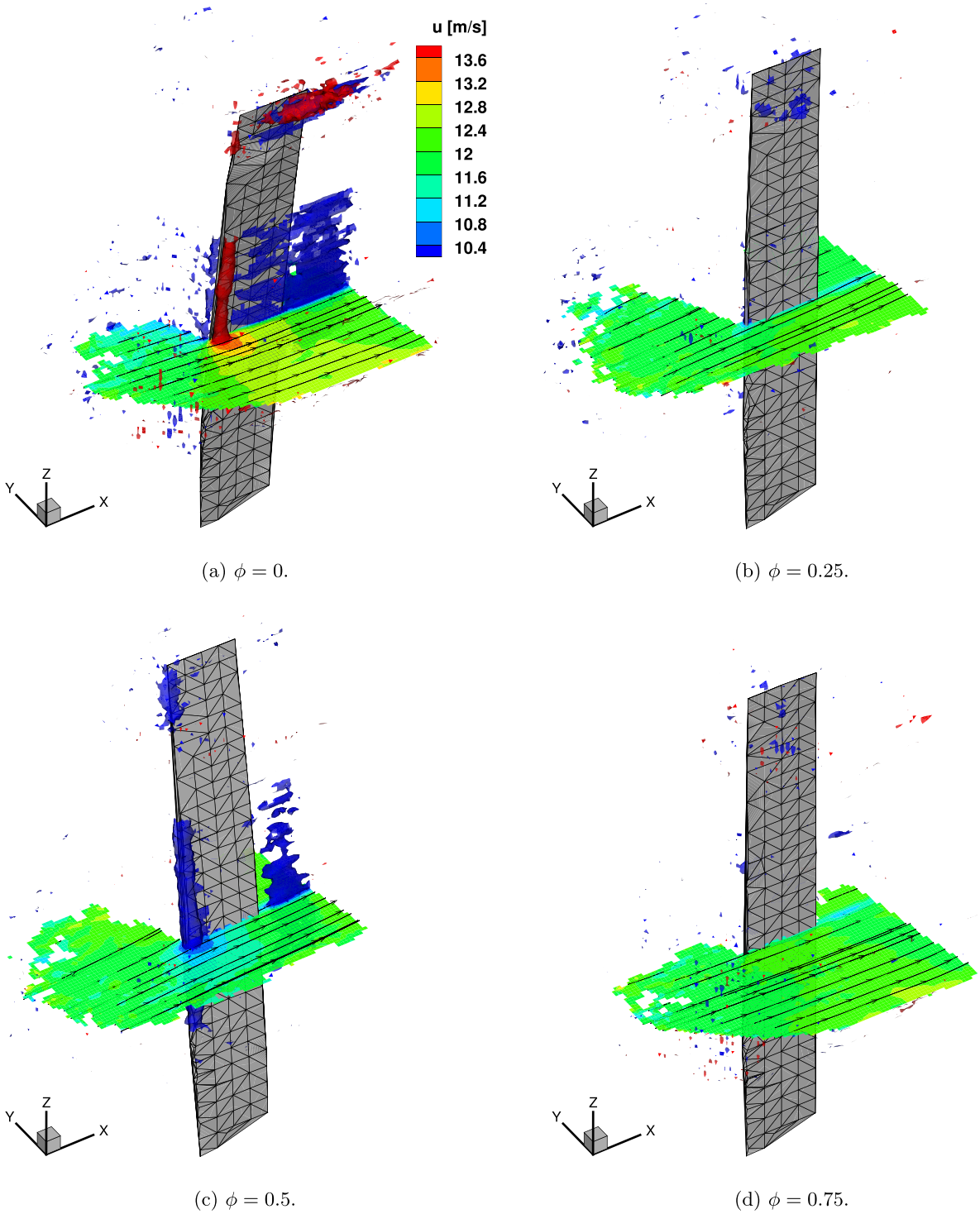

(a) $\phi = 0.$ (b) $\phi = 0.25.$

(c) $\phi = 0.5.$ (d) $\phi = 0.75.$

Figure 18. Phase-averaged 3D visualization of the flow and structure results at four phases of the oscillation cycle. Visualisation of the streamwise velocity components with streamlines, and iso-surfaces of $u = 10.4$ m s^{-1} (blue) and $u = 13.8$ m s^{-1} (red).

found 'beyond' the plate. However, because of the measurement errors in the position of both structural markers and flow particles, the latter can be found both before and beyond the plate. In the first case they are said to be valid particles, while in the second case they are called penetrating particles because they penetrate the surface of the structure. The proposed assessment is based on the ratio of penetrating particles with respect to the total number of particles within a certain distance from the plate.

The PTV-HFSB measurement set is used for this analysis. Two regions are investigated: one encompassing the half span of the plate and the other encompassing the tip of the plate.

The structural markers are phase-averaged and the plate surface is reconstructed by triangulating the resulting points.

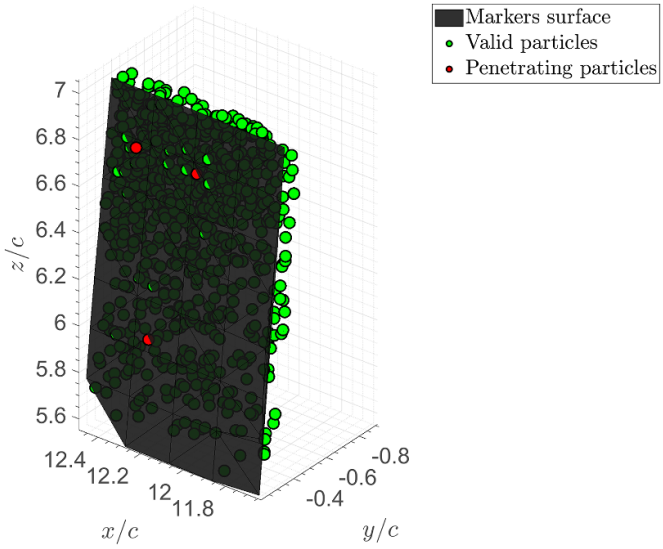

Figure 19. Illustration of valid flow particles and particles penetrating the solid surface of the plate.

Flow particles within a non-dimensional time window corresponding to the time between two successive recordings centered on the analyzed phase are considered. This set of particles is reduced by retaining only particles with an absolute distance from the triangulated surface below a threshold, which is defined as half of the spatial bin size. This is done to consider the limit case of an averaging bin with the centroid lying on the surface of the solid object. According to the size of the averaging bin used in section 5.3, the threshold is set to 14 mm.

At this point, it is possible to distinguish between valid and penetrating particles. An illustration of this distinction is given in figure 19 for the midspan region at phase $\phi = 0$.

Based on the distinction between valid and penetrating particles, it is possible to define a parameter called penetration probability and to investigate its variation over the cycle. The penetration probability is defined as the ratio between the number of penetrating particles N_{pen} and the total number of particles falling within the distance threshold N_{thr}:

$$P_{pen} = \frac{N_{pen}}{N_{thr}}. \tag{11}$$

Figure 20 shows the evolution of the penetration probability for both the midspan and the tip regions, providing also an indication of the plate's tip displacement corresponding to each phase. It is possible to observe that the level of penetration probability for tip particles is higher than for midspan particles. In fact, the mean and maximum penetration probability of midspan particles amount to 3.5% and 6.4%, respectively, while for the tip particles the corresponding values are 11.1% and 18.1%. This is in agreement with expectations, as the positional uncertainty of the CVV probe along its imaging direction is known to increase with the distance from the probe

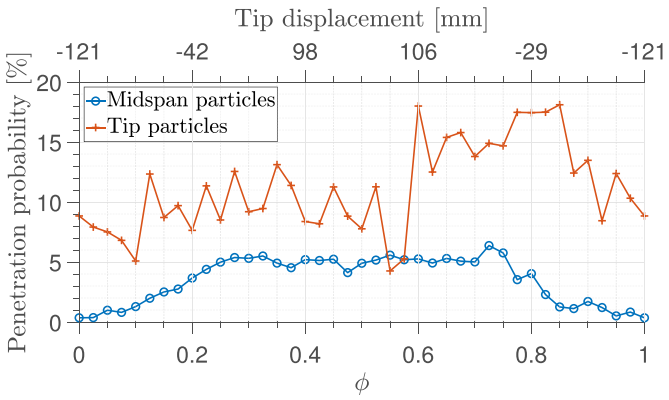

Figure 20. Penetration probability over the cycle.

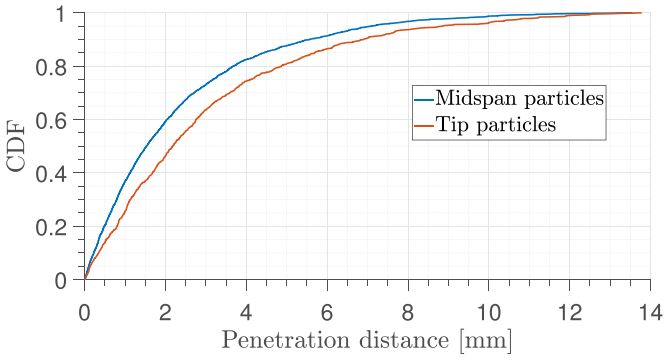

Figure 21. Cumulative distribution function of the penetration distance of the markers penetrating the structure.

itself and the maximum displacement of the plate at the tip is larger than the one at half of the span.

The penetration probability curve of midspan particles reveals also a higher level of penetration probability when the plate moves away from the probe (positive tip displacement). Once again, this is in agreement with the argument that the positional uncertainty of the CVV probe along its imaging direction increases with the distance from the probe itself. As a consequence, it is reasonable to expect that the further is the structure surface from the probe, the more particles penetrating the surface will be found. The same correlation between penetration probability and tip displacement is not observed for tip particles due to a lack of statistical convergence, given the smaller number of particles available at the tip.

Another important aspect to consider is the amount of penetration of the particles. This is evaluated in terms of the penetration distance, which is defined as the distance of the penetrating particles beyond the surface of the plate. The cumulative distribution function of the penetration distance for both midspan and tip particles over the entire cycle is calculated and plotted in figure 21. It can be observed that 90% of the particles in the midspan region have a penetration distance less than 5.6 mm (20% of the bin size), while in the tip region 90% of the particles have a penetration distance less

than 6.9 mm (25% of the bin size). Thus, the average smaller level of penetration probability for the midspan particles also coincides with a smaller penetration distance, which is in agreement with the argument of the increasing positional uncertainty of the CVV probe along the imaging direction.

6. Conclusions

A novel measurement approach is proposed for large-scale combined flow and structural measurements of periodic problems in a wind tunnel using robotic volumetric PTV. This approach exploits the particle tracking feature of the technique to track some fiducial markers painted on the surface of a structure in the same way as the flow particles. Image acquisition is initially carried out including both flow and structure tracers in the images. The two types of tracer are separated successively in the image pre-processing phase. A LPT algorithm is used to track the motion of the structural markers and the flow tracers. Further processing of the obtained tracks allows to achieve a three-dimensional combined measurement of phase-averaged flow velocities and structural displacements using a single measurement platform.

The measurement approach is demonstrated on a flexible plate excited by a periodic sinusoidal gust field. The phase-averaged near flow field over one side of the plate is studied, together with its dynamic response. A known technique based on polynomial regression for spatial ensemble averaging of flow tracks is extended to the temporal dimension to increase the spatial resolution of the measured phase-averaged velocity fields. This spatio-temporal ensemble averaging method is tested using a second-order polynomial and the results obtained prove the increased spatial resolution compared to the spatial only ensemble average. Furthermore, the analysis of the temporal kernel size reveals that a maximum value of 1/4 of the cycle period should be used to avoid a significant temporal modulation of the velocity.

The structural measurement is validated against a scanning vibrometer (SV). The instantaneous displacements are analyzed for three markers: one at the tip, one in the middle, and one at the root of the plate's span. The tip and midspan markers show a good agreement between the PTV and the SV measurements, with a bias error between 0.2% and 0.3% of the displacement amplitude and a random error between 0.7% and 0.8%. For the root marker a larger discrepancy is found because the amplitude of the displacement falls below the positional uncertainty of the CVV probe. Overall, the absolute bias and random errors of the markers' positions retrieved by robotic volumetric PTV are of the order of 0.1 and 0.5 mm, respectively. Furthermore, the motion of multiple markers is found to be consistent with the motion of a structural model of the plate based on its first three vibration modes. As a consequence, robotic volumetric PTV is found to be suitable for the measurement of large-scale structural displacements typical of dynamic aeroelastic phenomena such as gust encounters, while it would not be appropriate for measurements involving small-scale vibrations. Future studies could investigate more advanced methods for the processing of the structural tracks, such as the use of a FE model obtained from the regression of the markers' data to describe the displacement field over the entire plate, enforcing in this way a high degree of spatial and temporal consistency.

A study of the consistency of the fluid-structure measurement is finally carried out, initially presenting a visualization of the combined measurement that shows a good congruence between the structure and the boundary of the measured flow field. This is further assessed by investigating the number of flow particles penetrating the solid surface of the plate among the ones within a distance threshold corresponding to half the typical averaging bin size. The mean penetration probability over the cycle is found to be 3.5% for particles in the midspan region and 11.1% for particles in the tip region. Future research could be focused on the use of a flow averaging grid generated from the measured structure, in order to discard penetrating particles and consequently enforce hard compliance between flow and structure.

Overall, this work successfully demonstrates the feasibility of combined flow and structural measurement in wind tunnels by means of robotic volumetric PTV and its potential for large-scale aeroelastic experiments with measurement volumes in the order of 100 liters.

Data availability statement

The data that support the findings of this study are available upon reasonable request from the authors.

Acknowledgment

This work is partly funded by the European Union's Horizon 2020 research and innovation program project HOMER (Holistic Optical Metrology for Aero-Elastic Research), Grant Agreement No. 769237.

Appendix A. Derivation of reconstructed structure tracer size

The relation between the size of the reconstructed structure tracer and the viewing direction of the CVV system can be found by analyzing the geometry of the triangle constituting the first half of the parallelogram shown in figure 2(b). A detailed illustration of this triangle is presented in figure A1.

The reconstructed structure tracer size along the x-axis, d_x, is given by the projection of the segment $\overline{AC}$ onto the x-axis divided by the magnification factor:

$$d_x = \frac{\overline{AC}\sin(\pi/2-\theta)}{M} = \frac{\overline{AC}\cos\theta}{M}. \tag{A.1}$$

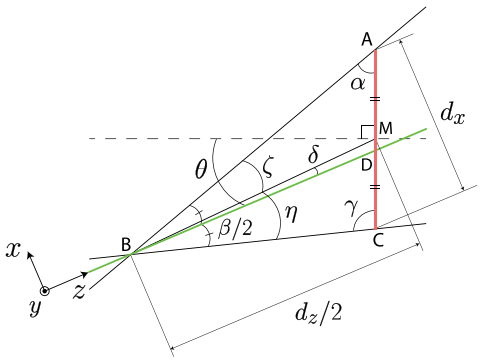

Figure A1. Schematic illustration of the geometric problem for the reconstruction of the structure particle. Structure tracer in red, z-axis of CVV system in green.

The projection of $\overline{AC}$ onto the x-axis corresponds to the projection of the particle image diameter d_τ onto the same axis. However, when deriving the mathematical expression of the projection, only the geometrical diameter should be projected onto the axis, as the diffraction-limited diameter d_{diff} remains unaltered independently of the viewing direction:

$$\begin{aligned}\overline{AC}\cos\theta &= \sqrt{\left(Md_p\cos\theta\right)^2 + d_{diff}^2} \\ &= \sqrt{\left(Md_p\cos\theta\right)^2 + \left(2.44f_{\#}\left(1+M\right)\lambda\right)^2}, \end{aligned} \tag{A.2}$$

where d_p is the physical size of the particle, $f_{\#}$ is the f-number of the lens and λ is the wavelength of the illumination used.

The size along the z-axis, d_z, corresponds to twice the projection of the segment $\overline{BM}$ onto the z-axis divided by the magnification factor:

$$d_z = \frac{2\overline{BM}\cos\delta}{M}. \tag{A.3}$$

The segment $\overline{BM}$ is the median of the side $\overline{AC}$ of the triangle and its length can be found as:

$$\overline{BM} = \frac{1}{2}\sqrt{2\overline{AB}^2 + 2\overline{BC}^2 - \overline{AC}^2}. \tag{A.4}$$

The sides $\overline{AB}$ and $\overline{BC}$ follow from the sine rule:

$$\begin{aligned}\overline{AB} &= \frac{\overline{AC}}{\sin\beta}\sin\gamma = \frac{\overline{AC}}{\sin\beta}\sin\left(\pi/2-\beta/2+\theta\right) \\ &= \frac{\overline{AC}}{\sin\beta}\cos\left(\beta/2-\theta\right); \end{aligned} \tag{A.5}$$

$$\begin{aligned}\overline{BC} &= \frac{\overline{AC}}{\sin\beta}\sin\alpha = \frac{\overline{AC}}{\sin\beta}\sin\left(\pi/2-\theta-\beta/2\right) \\ &= \frac{\overline{AC}}{\sin\beta}\cos\left(\theta+\beta/2\right). \end{aligned} \tag{A.6}$$

Substituting into (A.4), the segment $\overline{BM}$ reads:

$$\begin{aligned}\overline{BM} = \frac{\overline{AC}}{2}\Bigg(\frac{2}{\sin^2\beta}\Bigg(&\cos^2\left(\beta/2-\theta\right) \\ &+\cos^2\left(\beta/2+\theta\right)\Bigg)-1\Bigg)^{1/2}. \end{aligned} \tag{A.7}$$

Finally, δ is the angle between the median $\overline{BM}$ and the bisector $\overline{BD}$ and its tangent can be found as:

$$\tan\delta = \tan^2\frac{\beta}{2}\tan\left(\gamma/2-\alpha/2\right) = \tan^2\frac{\beta}{2}\tan\theta. \tag{A.8}$$

As a consequence, the ratio d_z/d_x reads:

$$\begin{aligned}\frac{d_z}{d_x} = \frac{\cos\delta}{\cos\theta}\Bigg(\frac{2}{\sin^2\beta}\Bigg(&\cos^2\left(\beta/2-\theta\right) \\ &+\cos^2\left(\beta/2+\theta\right)\Bigg)-1\Bigg)^{1/2}, \end{aligned} \tag{A.9}$$

where the angle δ is obtained as:

$$\delta = \tan^{-1}\left(\tan^2\frac{\beta}{2}\tan\theta\right). \tag{A.10}$$

Appendix B. Tracks connection and markers phase averaging

Several methods can be used to join together tracks belonging to the same marker. For the experiment realized in section 4, an algorithm employing polynomials for the prediction of the position of the marker was developed. The steps of the algorithm are conceptually illustrated in figure B1 and are explained in detail below.

Step 0. The first markers are initialized from the tracks belonging to the first time step of the acquisition. After this initialization step, the algorithm advances one time step at a time looking for new tracks to be assigned to the markers.

Step 1. New tracks starting at the analyzed time step are considered as candidates for the connection operation. From the entire set of markers, only the ones having the last time step prior to the current time step are considered for the analysis.

Step 2. A quadratic trajectory is fitted through the points of the first candidate marker (bold blue line in figure B1). The radius of search r_s defines the search region for the new tracks along the predicted trajectory. For each new track j, the mean distance $\mu_{1,j}$ between the predicted trajectory of the first candidate marker and the particles of the track is calculated, together with the related standard

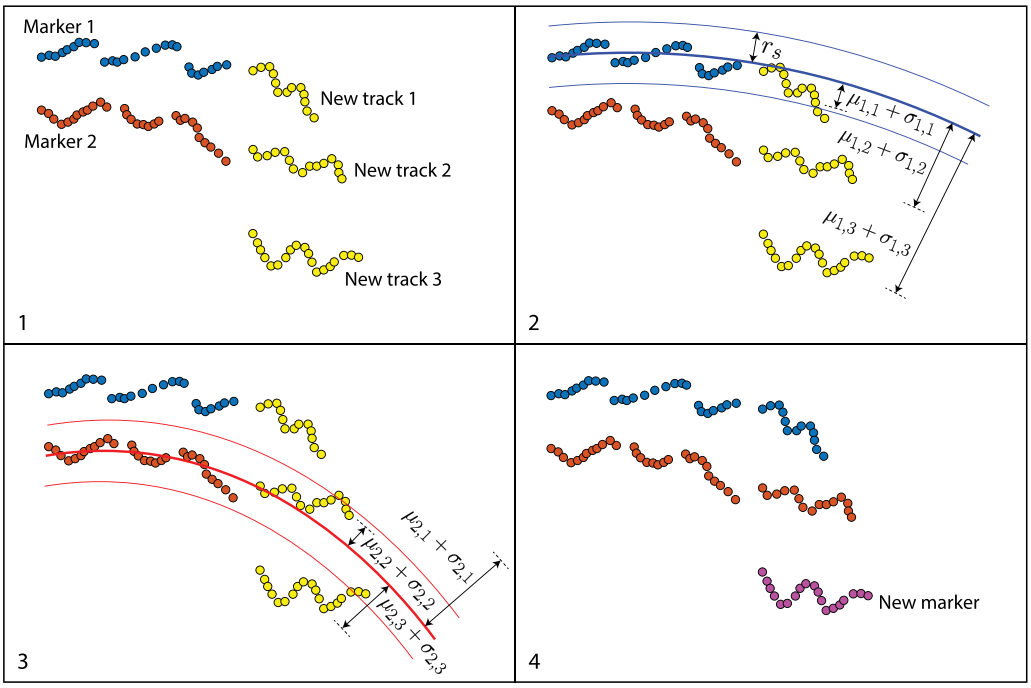

Figure B1. Illustration of the algorithm used for the operation of track connection.

deviation $\sigma_{1,j}$. Only the tracks having $\mu_{1,j}+\sigma_{1,j}<r_s$ are considered for the connection. If no track meets this condition, the marker is not further considered for the connection operation.

Step 3. Step 2 is repeated for each candidate marker.

Step 4. Each candidate marker i fulfilling the r_s criterion gets assigned the track having the smallest summation $\mu_{i,j}+\sigma_{i,j}$. The tracks not assigned to any marker become new markers. The algorithm advances to the next time step and resumes from step 1.

After the markers' information has been mapped from the real acquisition time to the corresponding phases of the cycle, their phase-averaged displacements are calculated using a technique that embeds the concept of track regularization. A sliding regression of a second-order polynomial is carried out over the coordinates of the markers. This step is analogous to the fitting of a quadratic trajectory during the track connection operation, however, this time the regression takes place over the non-dimensional time rather than the physical one, benefiting from the presence of a larger amount of particles. A kernel of 1/4 of the cycle was used for the results presented in section 5.

When different acquisitions are processed, the merging of coincident markers is achieved in the following way. A preliminary phase average is carried out separately for all markers. This means that coincident markers belonging to different acquisitions are initially kept distinct. The coincident markers are then identified by looking at the mean distance between couples of phase-averaged markers. The ones having a mean relative distance during the cycle smaller than a certain threshold are considered to be coincident. Subsequently, the raw information of those markers is merged and the final phase average takes place.

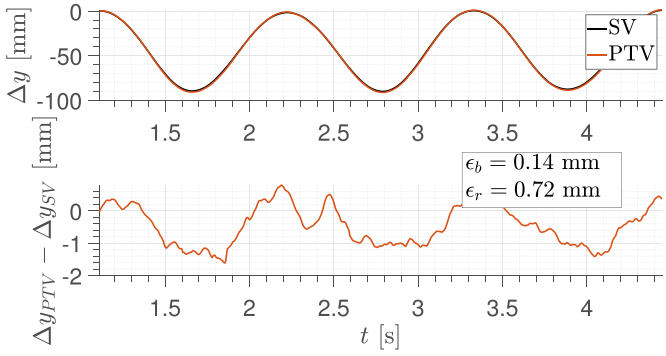

Figure C1. Time history of the instantaneous displacement obtained from robotic volumetric PTV and SV measurements for the tip marker (top) and of the related error (bottom). Only results from 3 gust cycles are shown.

Appendix C. Instantaneous displacements and accelerations of tip and root markers

In this appendix, the time histories of the displacements and accelerations of the tip marker and the root marker are shown, in comparison with the SV measurements.

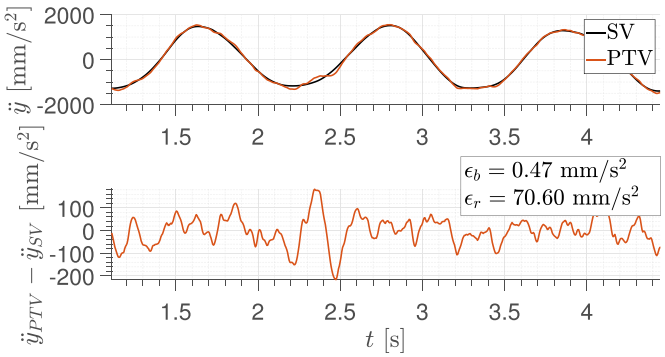

Figure C2. Time history of the instantaneous acceleration obtained from robotic volumetric PTV and SV measurements for the tip marker (top) and of the related error (bottom). Only results from 3 gust cycles are shown.

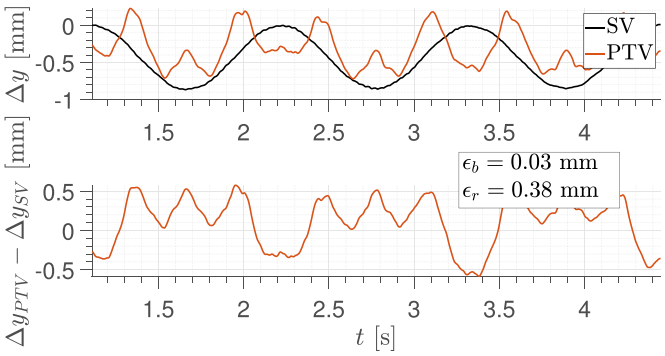

Figure C3. Time history of the instantaneous displacement obtained from robotic volumetric PTV and SV measurements for the root marker (top) and of the related error (bottom). Only results from 3 gust cycles are shown.

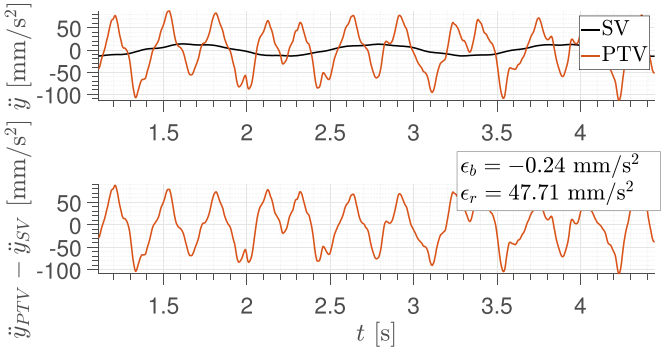

Figure C4. Time history of the instantaneous acceleration obtained from robotic volumetric PTV and SV measurements for the root marker (top) and of the related error (bottom). Only results from 3 gust cycles are shown.

ORCID iDs

Francesco M A Mitrotta https://orcid.org/0000-0001-8753-0749
Andrea Sciacchitano https://orcid.org/0000-0003-4627-3787

References

Adrian R J 1991 Particle-imaging techniques for experimental fluid mechanics *Annu. Rev. Fluid Mech.* **23** 261–304
Adrian R J and Westerweel J 2011 *Particle Image Velocimetry (Cambridge Aerospace Series)* (Cambridge: Cambridge University Press)
Agüera N, Cafiero G, Astarita T and Discetti S 2016 Ensemble 3D PTV for high resolution turbulent statistics *Meas. Sci. Technol.* **27** 124011
Ballmann J, Dafnis A, Korsch H, Buxel C, Reimerdes H G, Brakhage K H, Olivier H, Braun C, Baars A and Boucke A 2008 Experimental analysis of high Reynolds number structural dynamics in ETW (available at: https://arc.aiaa.org/doi/abs/10.2514/6.2008-841)
Bleischwitz R, de Kat R and Ganapathisubramani B 2017 On the fluid-structure interaction of flexible membrane wings forMAVs in and out of ground-effect *J. Fluids Struct.* **70** 214–34
Jux C, Sciacchitano A, Schneiders J F G and Scarano F 2018 Robotic volumetric PIV of a full-scale cyclist *Exp. Fluids* **59** 74
Kalmbach A and Breuer M 2013 Experimental PIV/V3V measurements of vortex-induced fluid–structure interaction in turbulent flow—a new benchmark FSI-PfS-2a *J. Fluids Struct.* **42** 369–87
Lancelot P, Sodja J and De Breuker R 2017a Investigation of the unsteady flow over a wing under gust excitation *17th Int. Forum on Aeroelasticity and Structural Dynamics, IFASD 2017* (*June*) vol 2017 ([IFASD-2017-185] Int. Forum on Aeroelasticity and Structural Dynamics (IFASD))
Lancelot P, Sodja J, Werter N and De Breuker R 2017b Design and testing of a low subsonic wind tunnel gust generator *Adv. Aircr. Spacecr. Sci.* **4** 125–44
Lynch K and Scarano F 2013 A high-order time-accurate interrogation method for time-resolved PIV *Meas. Sci. Technol.* **24** 035305
Mai H, Neumann J and Hennings H 2011 Gust response: a validation experiment and preliminary numerical simulations *15th Int. Forum on Aeroelasticity and Structural Dynamics* pp 1–20
Marimon Giovannetti L, Banks J, Turnock S R and Boyd S W 2017 Uncertainty assessment of coupled digital image correlation and particle image velocimetry for fluid-structure interaction wind tunnel experiments *J. Fluids Struct.* **68** 125–40
Martínez Gallar B, van Oudheusden B W, Sciacchitano A and Karásek M 2019 Large-scale volumetric flow visualization of the unsteady wake of a flapping-wing micro air vehicle *Exp. Fluids* **61** 16
Raffel M, Willert C, Scarano F, Kähler C, Wereley S and Kompenhans J 2018 *Particle Image Velocimetry: A Practical Guide (Experimental Fluid Mechanics)* (Cham: Springer Int. Publishing)
Ricketts R 1990 Experimental aeroelasticity—history, status and future in brief *31st Structures, Structural Dynamics and Conf.* (American Institute of Aeronautics and Astronautics)
Savitzky A and Golay M J E 1964 Smoothing and differentiation of data by simplified least squares procedures *Anal. Chem.* **36** 1627–39
Scarano F, Ghaemi S, Caridi G C A, Bosbach J, Dierksheide U and Sciacchitano A 2015 On the use of helium-filled soap bubbles for large-scale tomographic PIV in wind tunnel experiments *Exp. Fluids* **56** 42
Schanz D, Gesemann S and Schröder A 2016 Shake-the-box: Lagrangian particle tracking at high particle image densities *Exp. Fluids* **57** 70
Schanz D, Gesemann S, Schröder A, Wieneke B and Novara M 2012 Non-uniform optical transfer functions in particle

imaging: calibration and application to tomographic reconstruction *Meas. Sci. Technol.* **24** 024009
Schneiders J F G, Scarano F, Jux C and Sciacchitano A 2018 Coaxial volumetric velocimetry *Meas. Sci. Technol.* **29** 065201
Sciacchitano A and Scarano F 2014 Elimination of PIV light reflections via a temporal high pass filter *Meas. Sci. Technol.* **25** 084009
Sciacchitano A and Wieneke B 2016 PIV uncertainty propagation *Meas. Sci. Technol.* **27** 084006
Silva W, Perry B, Florance J, Sanetrik M, Wieseman C, Stevens W, Funk C, Hur J, Christhilf D and Coulson D 2012 An overview of the semi-span super-sonic transport (S4T) wind-tunnel model program (available at: https://arc.aiaa.org/doi/abs/10.2514/6.2012-1552)
Timpe A, Zhang Z, Hubner J and Ukeiley L 2013 Passive flow control by membrane wings for aerodynamic benefit *Exp. Fluids* **54** 1471
Wieneke B 2008 Volume self-calibration for 3d particle image velocimetry *Exp. Fluids* **45** 549–56
Zhang P, Peterson S D and Porfiri M 2019 Combined particle image velocimetry/digital image correlation for load estimation *Exp. Therm. Fluid Sci.* **100** 207–21